

Parametrized 3D models of neutrino-driven supernova explosions

Neutrino emission asymmetries and gravitational-wave signals

E. Müller, H.-Th. Janka, and A. Wongwathanarat

Max-Planck-Institut für Astrophysik, Karl-Schwarzschild-Straße 1, D-85748 Garching, Germany

Preprint online version: July 1, 2011

ABSTRACT

Time-dependent and direction-dependent neutrino and gravitational-wave (GW) signatures are presented for a set of three-dimensional (3D) hydrodynamic models of parametrized, neutrino-driven supernova explosions of non-rotating 15 and 20 M_{\odot} stars. We employ an approximate treatment of neutrino transport based on a gray spectral description and a ray-by-ray treatment of multi-dimensional effects. Due to the excision of the high-density core of the proto-neutron star and the use of an axis-free (Yin-Yang or "baseball") overset grid, the models can be followed from the post-bounce accretion phase through the onset of the explosion into more than one second of the early cooling evolution of the PNS without imposing any symmetry restrictions and covering a full sphere. GW and neutrino emission exhibit the generic time-dependent features already known from 2D (axi-symmetric) models. Violent non-radial hydrodynamic mass motions in the accretion layer and their interaction with the outer layers of the proto-neutron star together with anisotropic neutrino emission give rise to a GW signal with an amplitude of $\sim 5 - 20$ cm in the frequency range of 100–500 Hz. The GW emission from mass motions usually reaches a maximum before the explosion sets in. After the onset of the explosion the GW signal exhibits a low-frequency modulation, in some cases describing a quasi-monotonic growth, associated with the non-spherical expansion of the explosion shock wave and the large-scale anisotropy of the escaping neutrino flow. Variations of the mass-quadrupole moment due to convective activity inside the nascent neutron star contribute a high-frequency component to the GW signal during the post-explosion phase. The GW signals exhibit strong variability between the two polarizations, different explosion simulations and different observer directions, and besides common basic features do not possess any template character. The neutrino emission properties (fluxes and effective spectral temperatures) show fluctuations over the neutron star surface on spatial and temporal scales that reflect the different types of non-spherical mass motions in the supernova core, *i.e.*, post-shock overturn flows and proto-neutron star convection. However, because very prominent, quasi-periodic sloshing motions of the shock due to the standing accretion-shock instability are absent and the emission from different surface areas facing an observer adds up incoherently, the modulation amplitudes of the measurable neutrino luminosities and mean energies are significantly smaller than predicted by 2D simulations.

Key words. Supernovae: general — neutron stars: general

1. Introduction

The electromagnetic signature of core collapse supernovae has been exploited comprehensively and thoroughly by countless observations during the past decades, providing however only indirect information about the explosion mechanism. The up to now only recorded neutrino signal of a core collapse supernova (SN1987A) confirmed the idea that the collapse of the core of a massive star to neutron star densities provides the necessary energy for the explosion (Baade & Zwicky 1934). As gravitational waves (GW), the only other mean to probe the supernova engine besides neutrinos, are still to be detected, supernova modelers are preparing for such a prospective measurement by predicting the gravitational wave signature of core collapse supernovae with ever increasing realism (for reviews, see *e.g.*, Kotake et al. (2006); Ott (2009); Fryer & New (2011))

According the Einstein's theory of general relativity (GR) gravitational waves will be generated by any mass-energy distribution whose quadrupole (or higher) moment varies non-linearly with time. In core collapse supernovae this criterion is satisfied by time-dependent rotational flattening particularly during collapse and bounce, prompt post-shock convection, non-radial flow inside the proto-neutron star and in the neutrino-heated hot bubble, the activity of the standing accretion shock instability (SASI), asymmetric emission of neutrinos, and by asymmetries

associated with the effects of magnetic fields (for a recent review see, *e.g.*, Ott (2009), and references therein). While significant rotational deformation and dynamically relevant magnetic fields require particular progenitors which possess some (considerable) amount of rotational and magnetic energy or which must rotate fast and differentially (additional differential rotation develops during collapse) to amplify an initially weak magnetic field, all other processes are genuinely operative in any core collapse supernova.

Obviously, an adequate modeling of these effects and an accurate prediction of the GW signal ultimately requires three dimensional (3D) hydrodynamic simulations covering the collapse, bounce, and post-bounce evolution (at least) until a successful launch of the explosion and including a proper treatment of neutrino transport and the relevant microphysics. However, most studies of the past thirty years were either concerned with the collapse and bounce signal only (Müller 1982; Finn & Evans 1990; Mönchmeyer et al. 1991; Yamada & Sato 1994; Zwerger & Müller 1997; Rampp et al. 1998; Dimmelmeier et al. 2001, 2002; Kotake et al. 2003; Shibata 2003; Shibata & Sekiguchi 2004; Ott et al. 2004; Cerda-Duran et al. 2005; Saijo 2005; Shibata & Sekiguchi 2005; Kotake et al. 2006; Dimmelmeier et al. 2007; Ott et al. 2007; Dimmelmeier et al. 2008), or were restricted to axisymmetric (2D) models (Müller et al. 2004; Ott et al. 2006; Kotake et al.

2007; Marek et al. 2009; Murphy et al. 2009; Yakunin et al. 2010). Several authors also investigated the influence of magnetic fields on the GW signal during the collapse and early post-bounce evolution assuming axisymmetry (Kotake et al. 2004; Yamada & Sawai 2004; Kotake et al. 2005; Obergaulinger et al. 2006a,b) and no symmetry restriction at all (Scheidegger et al. 2008, 2010). The GW signal due to aspherical neutrino emission was first studied by Epstein (1978), and subsequently by Burrows & Hayes (1996); Müller & Janka (1997), and Kotake et al. (2007, 2009a,b, 2011), where the investigations by Müller & Janka (1997), and Kotake et al. (2009b, 2011) considered also 3D, *i.e.*, non-axisymmetric models.

Concerning 3D post-bounce models, the topic of the study presented here, Müller & Janka (1997) were the first to analyze the GW signature of 3D non-radial flow and anisotropic neutrino emission from prompt post-bounce convection in the outer layers of a proto-neutron star during the first 30 msec after supernova shock formation. Because of smaller convective structures and slower overturn velocities, the GW wave amplitudes of their 3D models are more than a factor of 10 smaller than those of the corresponding 2D ones, and the wave amplitudes associated with anisotropic neutrino emission are a factor of 10 larger than those due to non-radial gas flow. Fryer (2004) and Fryer et al. (2004) presented gravitational wave signals obtained from 3D core collapse simulations which extend up to 150 msec past bounce and were performed with a Newtonian Smoothed Particle Hydrodynamics code coupled to a three-flavor grey flux-limited diffusion neutrino transport scheme. GW emission occurs due to matter asymmetries arising from perturbations caused by precollapse convection, core rotation, and low-mode convection in the explosion engine itself, and due to anisotropic neutrino emission. Kotake et al. (2009b) simulated 3D mock-up models that mimic neutrino driven explosions aided by the SASI, and computed the GW signal resulting from anisotropic neutrino emission by means of a ray-tracing method in a post-processing step. They pointed out that the gravitational waveforms of 3D models vary much more stochastically than those of axisymmetric ones, *i.e.*, in 3D the GW signals do not possess any template character. However, when considering rotating models Kotake et al. (2011) argue that the GW waveforms resulting from neutrino emission exhibit a common feature, which results from an excess of neutrino emission along the spin axis due to the growth of spiral SASI modes. Scheidegger et al. (2008) simulated the collapse of two rotating and magnetized cores in 3D until several 10 msec past bounce applying a parametrized deleptonization scheme (Liebendörfer 2005) that is a good approximation until a few milliseconds past bounce. Scheidegger et al. (2010) extended their study by systematically investigating the effects of the equation of state, the initial rotation rate, and both the initial magnetic field strength and configuration on the GW signature. They also simulated three representative models until ~ 200 msec of post-bounce accretion (no development of explosions) incorporating a treatment for neutrino transport based on a partial implementation of the isotropic diffusion source approximation (Liebendörfer et al. 2009).

In the following we present the GW analysis of a set of parametrized 3D models of neutrino-powered supernova explosions covering the evolution from core bounce until ~ 1.4 s later, where the high-density inner core of the proto-neutron star (PNS) is excised and replaced by a time-dependent boundary condition and a central point mass. The neutrino transport is treated by an approximate solver based on a ray-by-ray treatment of the multi-dimensional effects (Scheck et al. 2006). As we analyze the GW signal arising from both non-radial mass

flow and anisotropic neutrino emission, we discuss the neutrino emission of these 3D models as well, and particularly address its multidimensional properties, some of which have previously been investigated in 2D by Janka & Mönchmeyer (1989a,b), Ott et al. (2008), Kotake et al. (2009a), Marek & Janka (2009), Marek et al. (2009), and Brandt et al. (2011).

Based on 2D simulations of rotational core collapse Janka & Mönchmeyer (1989a,b) pointed out that the energy output in neutrinos seen by an observer may vary as much as a factor of 3 with his inclination angle relative to the rotation axis, while for the neutrino energy much smaller angular variations are to be expected. Marek et al. (2009) and Marek & Janka (2009) found that neutrino luminosities and mean energies show quasi-periodic time variability in their 2D simulations of non-rotating and slowly rotating $15 M_{\odot}$ progenitors covering up to ~ 700 ms past bounce. Caused by the expansion and contraction of the shock in the course of SASI oscillations, the level of the fluctuations is $\lesssim 50\%$ for the luminosities and roughly 1 MeV for the mean neutrino energies. The luminosity fluctuations are somewhat bigger for ν_e and $\bar{\nu}_e$ than for heavy-lepton neutrinos. The neutrino quantities also depend on polar angle as a consequence of the preference of the SASI motions along the symmetry axis of the 2D models. Additional short-wavelength spatial variations of the average radiated energies and of the neutrino fluxes are caused by local downdrafts of accreted matter. This is in accordance with the findings of Müller & Janka (1997), who inferred from a post-processing analysis of the neutrino emission anisotropy that features in the GW signal of their 2D models of convection in the hot-bubble region are well correlated with structures in the neutrino signal. The features are associated with sinking and rising lumps of matter and with temporal variations of aspherical accretion flows towards the proto-neutron star. Kotake et al. (2009a) computed neutrino anisotropies with a ray-tracing scheme by post-processing their 2D SASI models and derived analytical expressions for evaluating GW signals for neutrinos in 3D models, too. A generalization of these expressions will be presented below. Brandt et al. (2011) performed 2D multi-group, multi-angle neutrino transport simulations for both a non-rotating and rapidly rotating $20 M_{\odot}$ model extending ~ 400 ms beyond bounce. Their simulations predict that the neutrino radiation fields vary much less with angle than the matter quantities in the region of net neutrino heating as most neutrinos are emitted from deeper radiative regions and as the neutrino energy density combines the specific intensities as integrals over sources at many angles and depths. The rapidly rotating model exhibits strong, flavor-dependent asymmetries in both peak neutrino flux and light curves, the peak flux and decline rate having pole-equator ratios $\lesssim 3$ and $\lesssim 2$, respectively. Brandt et al. (2011) also provide estimates of the detectability of neutrino fluctuations in IceCube and Super-Kamiokande as previously done by Lund et al. (2010) on the basis of the Marek et al. (2009) non-rotating models.

The paper is organized as follows: in Section 2 we discuss the numerical methods, the input physics, and the properties of the progenitor models and the set of 3D simulations we have analyzed. Section 3 contains a description of the formalism we used to extract the observable neutrino signal of our 3D models, and a discussion of some of its properties relevant for the corresponding GW signal. In Section 4 we give the formalism necessary to calculate the GW signature of 3D non-radial flow and anisotropic neutrino emission, and discuss the GW signature of the investigated 3D models. Finally, in Section 5 we summarize our results and discuss shortcomings and possible implications of our study.

2. Model setup

2.1. Code and computational grid

The 3D supernova models we have analyzed for their neutrino and GW signature have been simulated with the explicit finite-volume, Eulerian, multi-fluid hydrodynamics code PROMETHEUS (Fryxell et al. 1991; Müller et al. 1991a,b). This code integrates the multidimensional hydrodynamic equations using the dimensional splitting method of Strang (1968), the piecewise parabolic method of Collella & Woodward (1984), and a Riemann solver for real gases proposed by Colella & Glaz (1985). Inside grid cells with strong grid-aligned shocks fluxes computed from the Riemann solver are replaced by the AUSM+ fluxes of Liou (1996) in order to prevent odd-even decoupling (Quirk 1994). Nuclear species are advected using the Consistent Multi-fluid Advection (CMA) scheme of Plewa & Müller (1999).

The simulation code employs an axis-free overlapping “Yin-Yang” grid (Kageyama & Sato 2004) in spherical polar coordinates, which was recently implemented into PROMETHEUS, for spatial discretization (Wongwathanarat et al. 2010a). The Yin-Yang grid relaxes the CFL-timestep condition and avoids numerical artifacts near the polar axis. The grid consists of $400(r) \times 47(\theta) \times 137(\phi) \times 2$ cells corresponding to an angular resolution of 2° and covering the full 4π solid angle. The radial grid has an equidistant spacing of 0.03 km from the inner grid boundary out to $r = 80$ km (models W15 and N20; see Table 1) or 115 km (model L15; see Table 1), respectively. Beyond this radius the radial grid is logarithmically spaced. The outer radial grid boundary R_{ob} is at 18000 km, which is sufficiently far out to prevent the supernova shock from leaving the computational domain during the simulated epoch.

A central region, the dense inner core of the proto-neutron star (PNS) at $\rho \gtrsim 10^{12...13} \text{ g cm}^{-3}$, is excised from the computational domain and replaced by an inner time-dependent radial boundary condition and a point mass at the coordinate origin. Hydrostatic equilibrium is assumed at the inner radial grid boundary R_{ib} , which is thus a Lagrangian (co-moving) position, while a free outflow boundary condition is employed at the outer radial grid boundary (for more details, see Wongwathanarat (2011) and Wongwathanarat et al. (2010a)).

2.2. Input physics

Self-gravity is fully taken into account by solving Poisson’s equation in integral form using an expansion into spherical harmonics as in Müller & Steinmetz (1995). The monopole term of the potential is corrected for general relativistic effects as described in Scheck et al. (2006) and Arcones et al. (2007). The cooling of the PNS is prescribed by neutrino emission properties (luminosities and mean neutrino energies) as boundary condition at the inner radial grid boundary (for details, see Scheck et al. (2006)). The contraction of the PNS is mimicked by a radial grid movement. “Ray-by-ray” neutrino transport and neutrino-matter interactions are approximated as in Scheck et al. (2006) by radial integration of the one-dimensional (spherical), grey transport equation for all angular grid directions (θ, ϕ) independently. This approach allows for angular variations of the neutrino fluxes. The tabulated equation of state (EoS) of Janka & Müller (1996) is used to describe the stellar fluid. It includes arbitrarily degenerate and arbitrarily relativistic electrons and positrons, photons, and four predefined nuclear species (n, p, α , and a representative Fe-group nucleus) in nuclear statistical equilibrium.

Table 1. Some properties of the analyzed 3D models including the mass of the progenitor star M_{PS} , the mass of the neutron star M_{NS} , the time of explosion t_{exp} , and the explosion energy E_{exp} at the time t_f after bounce when we stopped the simulation. Note that $1 \text{ B} = 1 \text{ bethe} = 10^{51} \text{ erg}$.

Model	M_{PS} [M_{\odot}]	M_{NS} [M_{\odot}]	t_{exp} [ms]	E_{exp} [B]	t_f [s]
W15-2	15	1.37	248	1.13	1.3
W15-4	15	1.38	272	0.94	1.3
L15-2	15	1.51	381	1.74	1.4
L15-3	15	1.62	477	0.84	1.4
N20-2	20	1.28	265	3.12	1.3

2.3. Models

We have analyzed a set of 3D simulations (Wongwathanarat 2011; Wongwathanarat et al. 2010b, 2011) based on two $15 M_{\odot}$ progenitor models (W15 and L15), and a $20 M_{\odot}$ progenitor model (N20). The W15 model is obtained from the non-rotating $15 M_{\odot}$ progenitor s15s7b2 of Woosley & Weaver (1995), the L15 model from a star evolved by Limongi et al. (2000), and the N20 model from a SN 1987A progenitor of Shigezuma & Nomoto (1990). The progenitor models were evolved through collapse to 15 ms after bounce with the PROMETHEUS-VERTEX code in one dimension (A. Marek and R. Buras, private communication) providing the initial models for the 3D simulations. To break the spherical symmetry of the initial models, random seed perturbations of 0.1% amplitude are imposed on the radial velocity (v_r) field at the beginning of the 3D simulations. Explosions are initiated by neutrino heating at a rate that depends on suitable values of the neutrino luminosities imposed at the lower boundary chosen such that the desired value of the explosion energy is obtained. The evolution is followed until 1.3 s after bounce for the W15 and N20 progenitor models, while the L15 models are simulated until 1.4 s post-bounce. The GW analysis presented below comprises five models (see Table 1), where models W15-2 and W15-4 differ only by the initial seed perturbations. The explosion energies, E_{exp} , given in Table 1 are instantaneous values at the end of the simulations ($t = t_f$), adding up the total energies (kinetic + internal + gravitational) in all zones where the sum of these energies is positive. The explosion time, t_{exp} , is defined as the time when this sum exceeds a value of 10^{48} erg , roughly corresponding to the time when the average shock radius is 400 to 500 km (see, however, Pejcha & Thompson (2011) for an alternative definition of the time of the onset of the explosion).

3. Neutrino signal

The non-radial motions caused by the SASI and convection in the neutrino-heated hot-bubble as well as by convection inside the proto-neutron star (driven by Ledoux unstable lepton gradients) give rise to a time-dependent, anisotropic emission of neutrinos of all flavors, and thus to the emission of gravitational waves (Epstein 1978; Burrows & Hayes 1996; Müller & Janka 1997; Kotake et al. 2007, 2009a,b), as discussed in Sect. 4. We have analyzed this emission for the 3D models discussed above (see Sect. 2.3), particularly addressing its multidimensional properties.

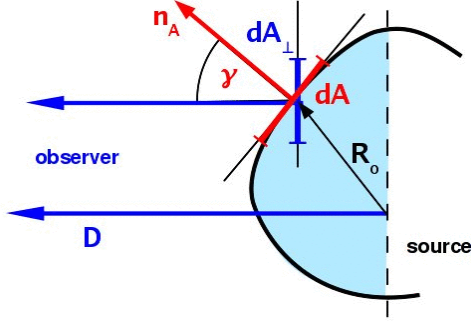


Fig. 1. Sketch illustrating the various quantities involved when deriving the observable luminosity of a radiating source, whose visible surface is shaded in blue.

3.1. Formalism

To derive *observable luminosities* of an emitting source we consider an observer located at large distance D from that source (see Fig. 1). According to definition the flux measured by the observer is given by the following integral over the opening angle subtended by the emitting surface (not necessarily a sphere) at the position of the observer:

$$F(D, t) = \oint d\omega \mu I(D, \omega, t), \quad (1)$$

where μ is the cosine of the angle between the direction of the radiation and the line of sight (between the observer and the center of the source), ω denotes the radiation direction at the observer's location (defined by a pair of angles), and $d\omega$ is the solid angle element around the radiation direction ω . We note that here and in the following we suppress the dependence of the intensity on the neutrino energy and assume that energy-integrated quantities are considered (the outlined formalism, however, is valid also for an energy-dependent treatment). The integration over ω at the observer's location can be substituted by an integration over the emitting surface of the source, because the radiation intensity is constant along rays, *i.e.*,

$$I(D, \omega, t) = I_0(\mathbf{R}_o, \omega_o, t) \quad (2)$$

for any ray arriving at the observer from the source (and zero otherwise), where \mathbf{R}_o denotes the position of a surface element of the emitting surface in the source frame and ω_o the direction of the radiation field at that position towards the observer. Note that we ignore in Eq. (2) the trivial effect that the time t for I_0 relative to the time for I is subject to a retardation.

For a distant observer $D \gg \max\{|\mathbf{R}_o|\}$ holds, *i.e.*, the value of μ is very close to one for the whole emitting surface. Denoting the solid angle subtended by a surface element of the emitting surface by $d\omega$, we have $d\omega = dA_{\perp}/D^2$, where $dA_{\perp} = \cos \gamma dA$ is the projected area of this surface element perpendicular to the line of sight, when γ is the angle between the normal unit vector \mathbf{n}_A of the emitting surface element dA and the line of sight (see Fig. 1). Hence, we obtain for the observable luminosity the expression

$$L_o(t) = 4\pi D^2 F(D, t) = 4\pi \int_{\text{vis. surf.}} dA \cos \gamma I_o(\mathbf{R}_o, \omega_o, t). \quad (3)$$

Assuming that the *neutrino intensity* I_o is axisymmetric around the normal vector \mathbf{n}_A at all points \mathbf{R}_o implies that the

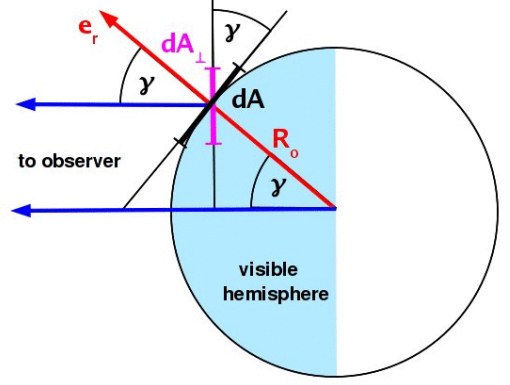


Fig. 2. Sketch illustrating the various quantities involved when deriving the observable luminosity for the particular case of a radiating sphere, whose visible hemisphere is shaded in blue..

direction-dependence of the intensity I_o is described by the direction angle γ only (see Fig. 1), *i.e.*, $I_o = I_o(\mathbf{R}_o, \gamma, t)$, and that the flux direction is given by \mathbf{n}_A . Accordingly, we obtain

$$I_o(\mathbf{R}_o, \gamma, t) = \frac{F_o(\mathbf{R}_o, t)}{2\pi} \left(1 + \frac{3}{2} \cos \gamma\right), \quad (4)$$

where F_o is the flux density normal to the emitting surface element dA . This expression corresponds to the limb-darkening law $I_E(\cos \gamma)/I_E(1) = (2/5)(1 + 3/2 \times \cos \gamma)$ that can be derived on grounds of the Eddington approximation (see, *e.g.*, Mihalas (1978), page 61). Since $I_o \geq 0$, Eq. (4) is strictly valid only when $\cos \gamma \geq -2/3$, which holds for the whole visible surface, where the integration is performed for $0 \leq \cos \gamma \leq 1$.

Inserting Eq. (4) into Eq. (3) we find for the observable neutrino luminosity the expression

$$L_o(t) = 2 \int_{\text{vis. surf.}} dA \cos \gamma F_o(\mathbf{R}_o, t) \left(1 + \frac{3}{2} \cos \gamma\right). \quad (5)$$

We further define an *observable mean neutrino energy* according to

$$\langle E \rangle_o(t) = \frac{L_o(t)}{L_{n,o}(t)}, \quad (6)$$

where

$$L_{n,o}(t) = 2 \int_{\text{vis. surf.}} dA \cos \gamma \frac{F_o(\mathbf{R}_o, t)}{\epsilon(\mathbf{R}_o, t)} \left(1 + \frac{3}{2} \cos \gamma\right) \quad (7)$$

is the observable *neutrino number flux* with ϵ being the mean energy of the neutrino energy spectrum radiated from point \mathbf{R}_o .

Our 3D radiation hydrodynamics code computes the time-dependent *neutrino energy flux density*, $F_o(\mathbf{R}_o, t)$, and *neutrino number flux density*, $F_{n,o}(\mathbf{R}_o, t)$, through a sphere of radius $R_o = |\mathbf{R}_o|$ depending on angular position $\Omega \equiv (\theta, \phi)$, but actually stores the related quantities

$$\Lambda(\Omega, t) \equiv 4\pi R_o^2 F_o(\Omega, t), \quad (8)$$

and

$$\Lambda_n(\Omega, t) \equiv \frac{\Lambda(\Omega, t)}{\epsilon(\Omega, t)} = 4\pi R_o^2 F_{n,o}(\Omega, t), \quad (9)$$

because these quantities are constant in the free-streaming region. Note that due to the ray-by-ray transport approximation used in our simulations both the neutrino energy flux and the neutrino number flux are purely radial.

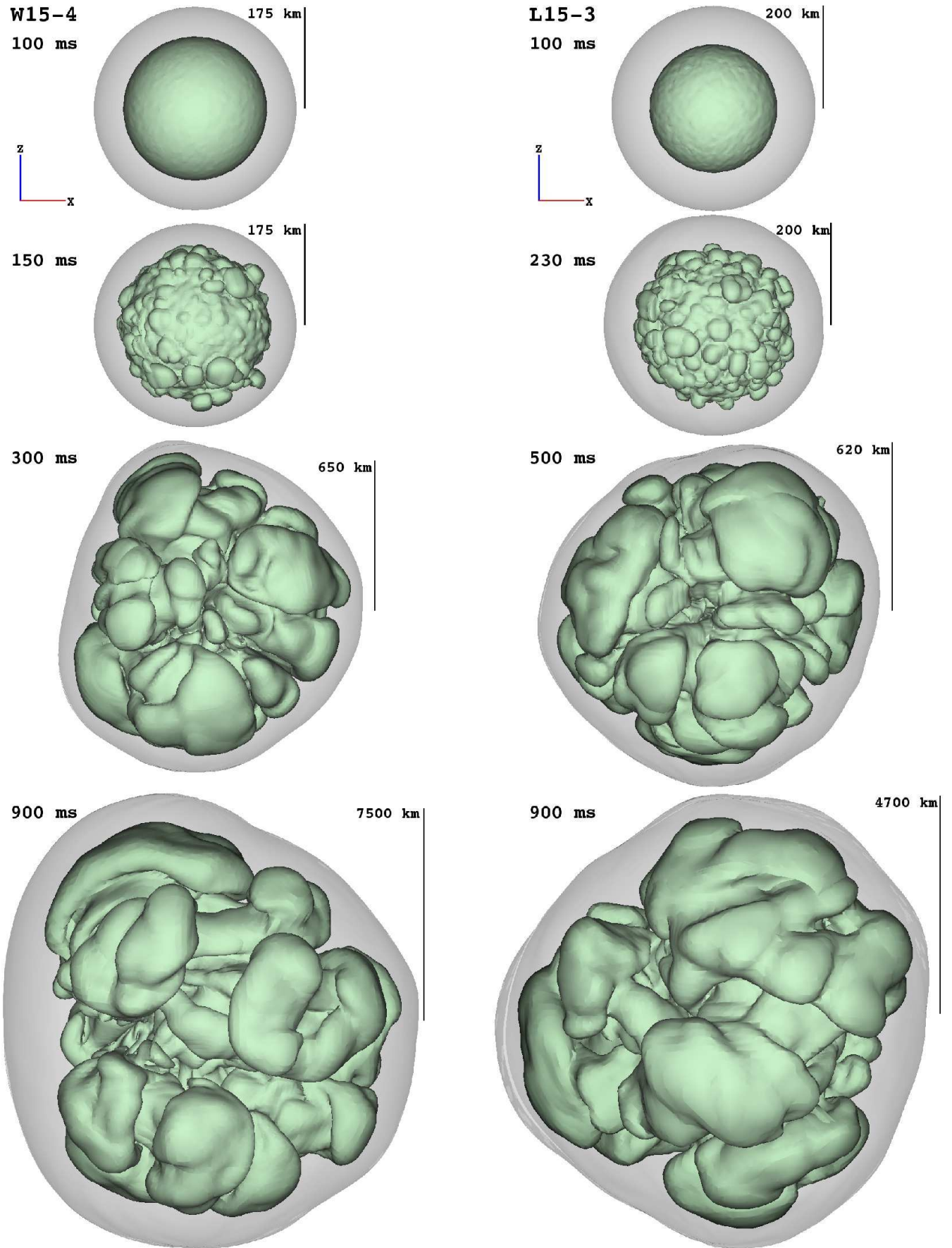


Fig. 3. Snapshots of models W15-4 (left) and L15-3 (right) illustrating the four phases characterizing the evolution of our 3D models (see text for details). Each snapshot shows two surfaces of constant entropy marking the position of the shock wave (grey) and depicting the growth of non-radial structures (greenish). The time and linear scale are indicated for each snapshot.

Using Eqs. (8) and (9), and the fact that $dA = R_o^2 d\Omega$ with $d\Omega = \sin\theta d\theta d\phi$ for the special case of an emitting sphere of radius R_o (see Fig. 2), we can rewrite the general expression for the observable neutrino luminosity given in Eq. (5) in the form

$$L_o(t) = \frac{1}{2\pi} \int_{\text{vis.hem.}} d\Omega \cos\gamma \Lambda(\mathbf{\Omega}, t) \left(1 + \frac{3}{2} \cos\gamma\right) \quad (10)$$

and that of the observable neutrino number flux given in Eq. (7) in the form

$$L_{n,o}(t) = \frac{1}{2\pi} \int_{\text{vis.hem.}} d\Omega \cos\gamma \Lambda_n(\mathbf{\Omega}, t) \left(1 + \frac{3}{2} \cos\gamma\right), \quad (11)$$

where in both cases the integration is performed over the visible hemisphere.

For the evaluation of the gravitational wave amplitude in Sect. 4.1.2 we will also need the quantity

$$\frac{d\Lambda(\mathbf{\Omega}, t)}{d\Omega} \equiv F_o(\mathbf{\Omega}, t) R_o^2 \quad (12)$$

and the corresponding angle-integrated quantity

$$\Lambda(t) \equiv \oint_{\text{surf.}} d\Omega \frac{d\Lambda(\mathbf{\Omega}, t)}{d\Omega} = \frac{1}{4\pi} \oint_{\text{surf.}} d\Omega \Lambda(\mathbf{\Omega}, t). \quad (13)$$

For the later discussion of the results we finally define the *surface-averaged neutrino flux density*

$$\langle F_o \rangle(t) \equiv \frac{1}{4\pi} \oint_{\text{surf.}} d\Omega F_o(\mathbf{\Omega}, t) \equiv \frac{1}{4\pi R_o^2} \frac{d\mathcal{E}(t)}{dt}, \quad (14)$$

where

$$\frac{d\mathcal{E}(t)}{dt} = \oint_{\text{surf.}} d\Omega \frac{d\Lambda(\mathbf{\Omega}, t)}{d\Omega} = \Lambda(t) \quad (15)$$

is the total energy loss rate at time t from the supernova core to all directions, which (because of the flux variations over the sphere) is not directly observable quantity.

We have also analyzed the evolution of the neutrino flux asymmetry by calculating the angular pseudo-power spectrum of the neutrino energy flux variation

$$\delta_\Lambda(\mathbf{\Omega}, t) \equiv \frac{\Lambda(\mathbf{\Omega}, t) - \Lambda(t)}{\Lambda(t)}, \quad (16)$$

where $\Lambda(\mathbf{\Omega}, t)$ and $\Lambda(t)$ are defined in Eqs. (8) and (13), respectively. The pseudo-power spectrum is given by the decomposition of $\delta_\Lambda(\mathbf{\Omega}, t)$ in spherical harmonic coefficients

$$\Lambda_m(t) = \oint d\Omega \delta_\Lambda(\mathbf{\Omega}, t) Y_{lm}^*(\mathbf{\Omega}), \quad (17)$$

where $Y_{lm}^*(\mathbf{\Omega})$ is the respective (complex conjugate) spherical harmonics. For our mode analysis we actually used the pseudo-power coefficients $C_l \equiv |\Lambda_{00}|^2$, and

$$C_l \equiv \frac{1}{2l+1} \left(|\Lambda_{l0}|^2 + 2 \sum_{m=1}^{m=l} |\Lambda_{lm}|^2 \right) \quad (18)$$

for $l > 0$, respectively.

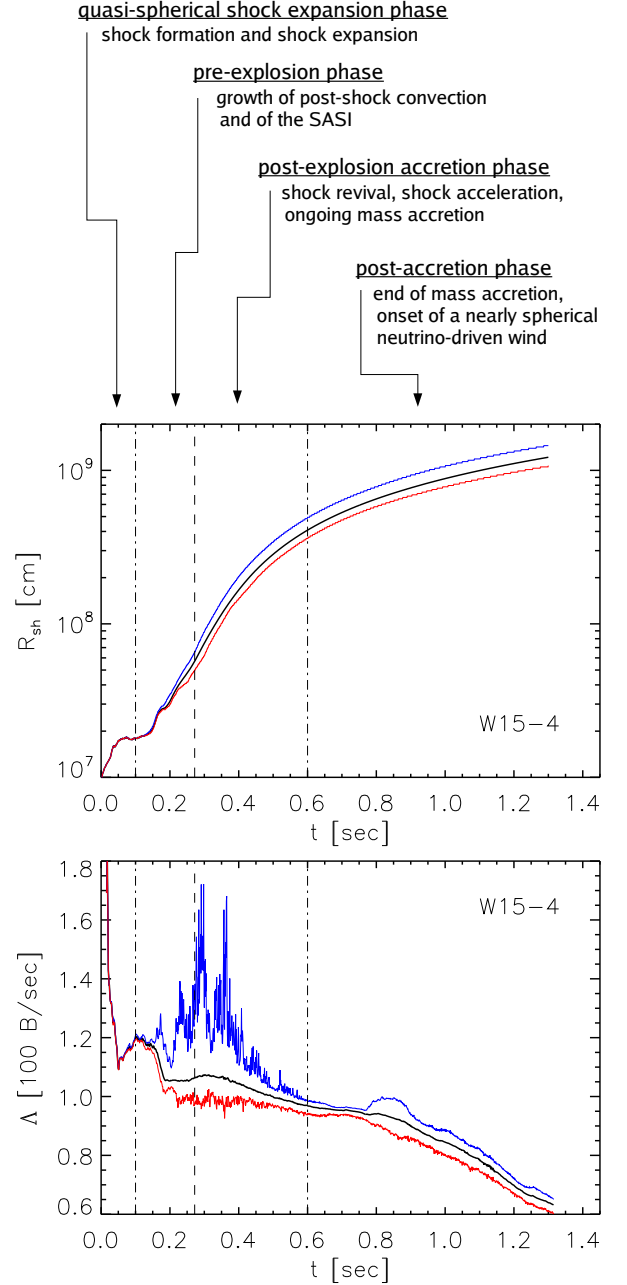


Fig. 4. Shock radius (top) and total (*i.e.*, summed over all flavors) energy loss rate due to neutrinos (bottom) as functions of time for model W15-4. In the upper panel, the black curve shows the angle-averaged mean shock radius, the blue (red) curve gives the maximum (minimum) shock radius, and the vertical dashed line marks the time of the onset of the explosion as defined in Sect. 2.3. In the lower panel, the blue and red curves show the time evolution of $\Lambda_{\max}(\mathbf{\Omega}, t)$ and $\Lambda_{\min}(\mathbf{\Omega}, t)$, the maximum and minimum value of $\Lambda(\mathbf{\Omega}, t)$ (Eq. 8) on a sphere of 500 km radius, respectively. The black line gives the corresponding surface-averaged value $\Lambda(t)$ (Eq. 13). Note that the luminosities imposed at the inner radial grid boundary are kept constant during the first second and later are assumed to decay like $t^{-2/3}$.

3.2. Results

The evolution of our models can be divided into four distinct phases (Figs. 3, 4).

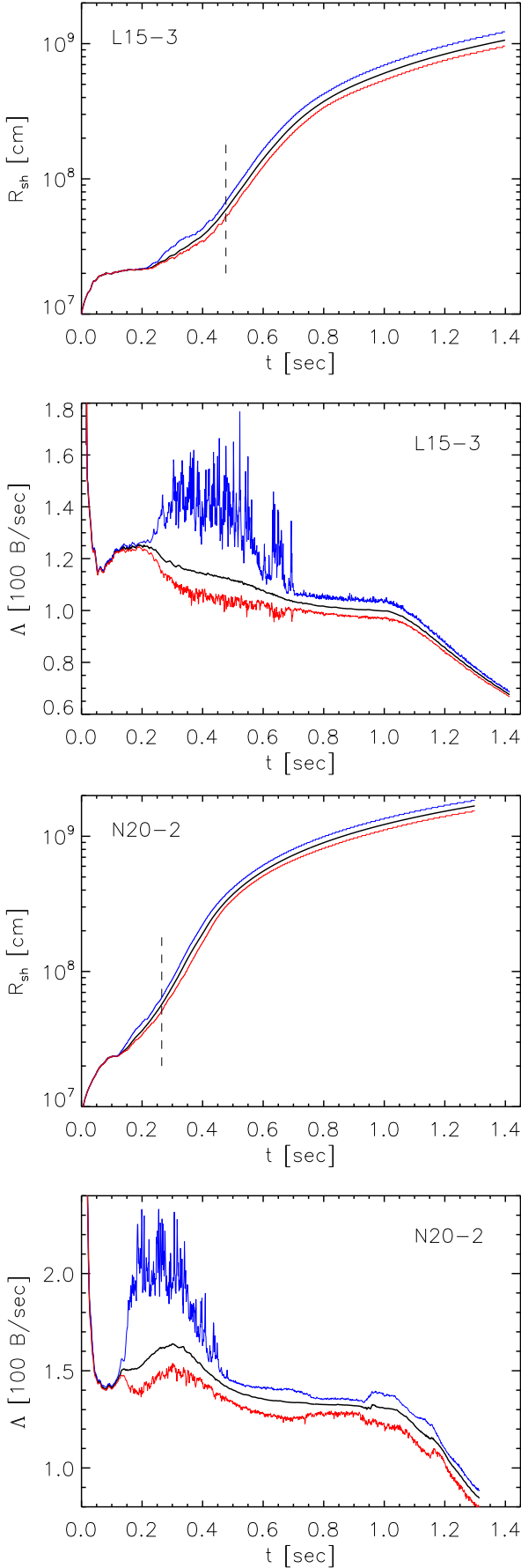


Fig. 5. Same as Fig. 4 but for models L15-3 (uppermost two panels) and N20-2 (lowermost two panels), respectively.

- (1) The first phase, the *quasi-spherical shock-expansion phase* (Fig. 3, top row), lasts from shock formation shortly after core bounce to 80 – 150 msec, when convection sets in. During this phase the shock rapidly propagates out to a radius of ~ 200 km, where its expansion comes to a halt.
- (2) The second phase, the hydrodynamically vigorous *pre-explosion phase*, comprises the growth of post-shock convection and of the standing accretion shock instability, SASI (Fig. 3, second row from top).
- (3) The *post-explosion accretion phase* begins when energy deposition by ν -heating in the post-shock layers becomes sufficiently strong, and the total energy in the post-shock region ultimately becomes positive (see Sect. 2.3 for a definition). During this phase the shock accelerates outward while gas is still accreted onto the PNS. This process is commonly called “shock revival” (Fig. 3, third row from top).

Non-radial instabilities during the latter two stages cause considerable temporal and angular fluctuations of the neutrino energy flux density as illustrated in Figs. 4 - 6. Besides the evolution of the shock radius, the figures show the surface-averaged neutrino light curve $\Lambda(t)$, *i.e.*, the total energy loss due to neutrinos versus time (Eqs. 13, 15), together with the time evolution of the maximum and minimum values of $\Lambda(\Omega, t)$ (Eq. (8)); the numerical evaluation is performed on an arbitrarily chosen sphere of 500 km radius). Distinct and large-amplitude spikes in $\Lambda_{\max}(\Omega, t)$ are visible for several 100 msec and reflect violent post-shock convection, possible SASI activity, and anisotropic accretion fluctuations after the onset of the explosion. We have marked the explosion time t_{exp} (see Section 2.3, and Table 1) by a vertical dashed line in Figs. 4 and 5. The post-explosion accretion phase lasts until ~ 500 msec (models W15-4 and N20-2) or ~ 700 msec (model L15-3) depending on the progenitor.

- (4) During the *post-accretion phase*, the fourth and final phase characterizing the evolution of our models (Fig. 3, bottom row), gas infall to the proto-neutron star has come to an end and the newly formed neutron star loses mass at a low rate in a nearly spherical neutrino-driven wind. We find considerably less temporal variability and a smaller level of angular variation ($\lesssim 10\%$) of the neutrino emission during this fourth phase (Figs. 4 - 6).

While in model L15-3 the amplitudes of the neutrino emission fluctuations decrease continuously, the other two models exhibit growing temporal emission variations (though at a smaller level than the earlier variability) during a later stage (notice the decrease/increase in $\Lambda_{\max} - \Lambda_{\min}$ in Figs. 4 and 5), which might be considered as a fifth evolutionary phase. This phase is associated with growing convective activity below the neutrinosphere. This PNS convection develops more or less strongly in the different models depending on the location of the convectively unstable region relative to the inner radial boundary of our computational domain.

We have evaluated the time evolution of the neutrino energy flux asymmetry by producing 4π -maps that show the relative angular variation $\Delta F_o / \langle F_o \rangle$ of the total (*i.e.*, sum of all neutrino flavors) neutrino energy flux density across a sphere (normalized to the surface-averaged flux density; Eq. 14). Several snapshots of this evolution are shown for model W15-4 in Fig. 6. The evolution of the typical angular scales of the fluctuations is reflected by the pseudo-power spectrogram of the electron neutrino energy flux variation (Eq. 16) in Fig. 7, top panels, which give the color-coded pseudo-power coefficient distribution normalized to the maximum value versus time. The variation of the pseudo-

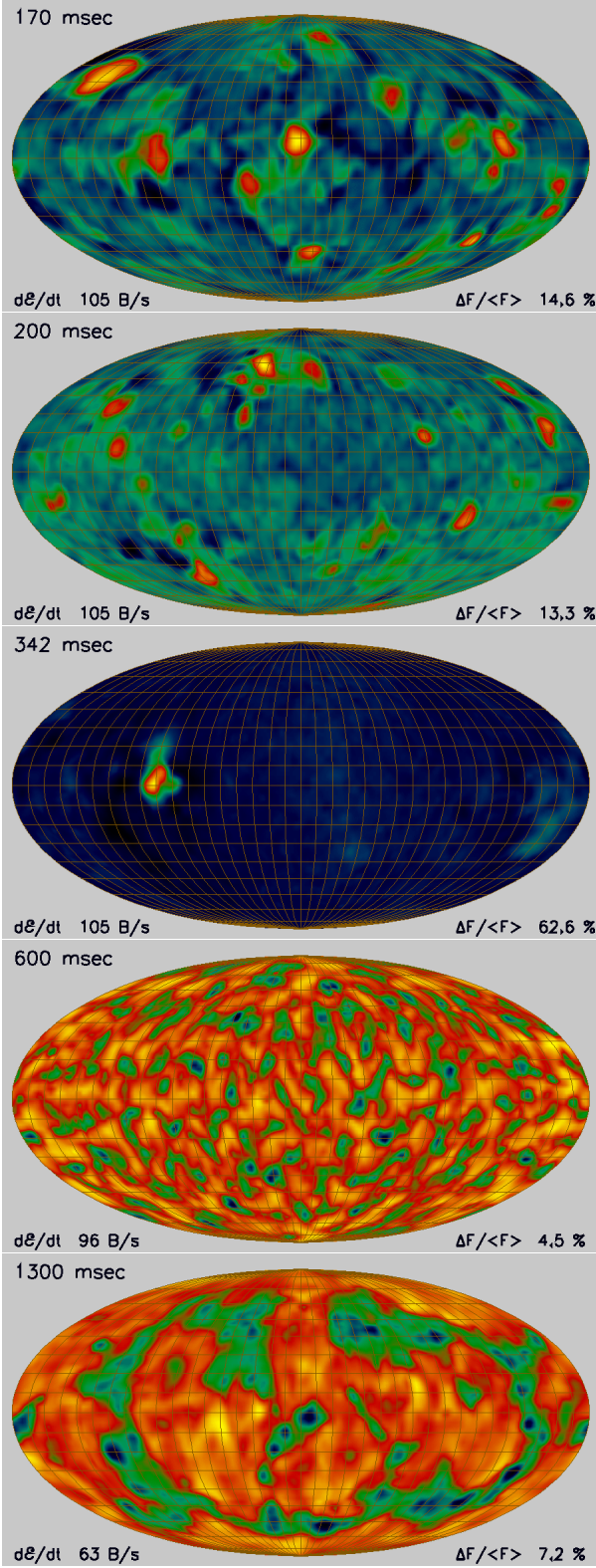


Fig. 6. Neutrino flux asymmetry at 170 msec, 200 msec, 342 msec, 600 msec, and 1.3 sec (from top to bottom), respectively. The 4π -maps show the relative angular variation $\Delta F_o/\langle F_o \rangle$ of the total (*i.e.*, sum of all neutrino flavors) neutrino energy flux density over a sphere (normalized to its angular average) for model W15-4. The maximum value is given in the lower right corner of each panel. Regions of higher emission are shown in bright yellow, while orange, red, green, and blue colors indicate successively less emission. The total energy loss rate due to neutrinos is given in the lower left corner.

power coefficients with angular mode number is shown in Fig. 8 at selected times of 200 ms (blue), 400 ms (red), and 1000 ms (black).

During the quasi-spherical shock expansion phase the level of angular fluctuations of F is small ($\lesssim 10^{-2}$), while the fluctuation amplitudes of the total neutrino energy flux density reach a level of several 10% during the hydrodynamically vigorous second phase and the post-explosion accretion phase, where a few distinct regions or even single spots with an angular size of 10° to 20° dominate the emission (Fig. 6, panels 2 and 3). The mode number l of the dominant angular perturbation scale is of no relevance during the first phase, as the maximum pseudo-power coefficient C_l^{\max} (see Eq. 18) is tiny $\lesssim 10^{-6}$ (Fig. 7, middle panels), *i.e.*, the dominating $l = 2$ and $l = 4$ modes visible in the upper panels of Fig. 7 only reflect tiny angular perturbations imprinted presumably by the computational grid. When neutrino heating eventually causes significant non-radial flow during the second and third phases, C_l^{\max} rises sharply to a level of $\sim 10^{-3}$ (Fig. 7, middle panels), and the relative angular variations of the electron neutrino flux density grow to the several ten percent level (Fig. 7, bottom panels). The latter quantity gives the maximum minus the minimum flux density on the sphere divided by the angle-averaged flux density in percent. Compared to the *total* neutrino emission in Figs. 4 - 6, the temporal and angular variations in different directions are even more pronounced when considering the energy flux of the electron neutrinos or electron anti-neutrinos alone (Fig. 7), where angular variations can exceed 100% in all models during the pre-explosion and accretion phases, and peak values are close to 200% during short episodes (Fig. 7, lower panels).

During the vigorous pre-explosion phase including the post-explosion accretion stage, electron neutrinos and antineutrinos dominate the angular flux variations, while muon and tau neutrinos (accounting for roughly 50% of the total luminosity) exhibit essentially isotropic emission in all directions. The reason of this finding is the fact that almost exclusively ν_e and $\bar{\nu}_e$ are produced by efficient charged-current reactions in the accretion region perturbed by non-radial fluid flows. The spectrogram of the two phases is characterized by initially very small-scale angular variations with $l \gtrsim 12$, which are associated with the onset of the Rayleigh-Taylor overturn activity, and which merge to continuously larger angular structures that correspond to $l \approx 1 \dots 4$ modes towards the end of the accretion period at $0.4 - 0.6$ s (depending on the model). This evolution is accompanied by a steady decrease of C_l^{\max} to a level of $\sim 10^{-5}$ and a reduction of the electron neutrino flux density variations from values well beyond 100% to a level of $\sim 10\%$, only (see Fig. 7, left panels).

When neutrino-energy deposition in the post-shock layers becomes sufficiently strong and the explosion is eventually launched at about 250 to 500 msec (depending on the model; Table 1), subsequent radial shock expansion rapidly diminishes the activity of the SASI and freezes post-shock convection. Single, longer lasting downdrafts of accretion flows are associated with isolated hot spots, where the variations of the total flux density can reach peak amplitudes up to $\sim 70\%$ (Fig. 6, panel 3). When accretion has ended, the amplitude of the angular variations of the total neutrino energy flux reduces to a level of a few percent (Figs. 4, 5), and the angular pattern of the emission becomes more uniform over the sphere consisting of many spots with an angular size of $\sim 30^\circ$ (Fig. 6, panel 4).

In the early post-accretion phase of model W15-4, $0.6 \text{ s} \lesssim t \lesssim 0.8 \text{ s}$, the spectrogram indicates the presence of small-amplitude ($C_l^{\max} \lesssim 10^{-4}$), small-angular size ($l \gtrsim 10$) perturbations in the electron neutrino energy flux caused by some low-

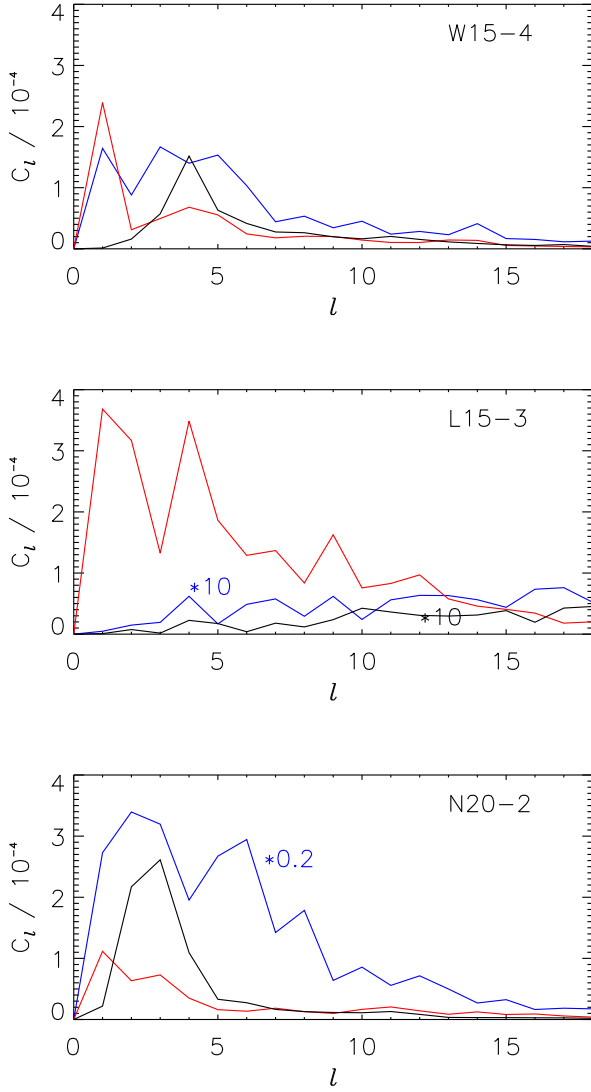


Fig. 8. Pseudo-power coefficients C_l^{\max} of the electron-neutrino flux density as functions of angular mode number l at 200 ms (blue), 400 ms (red), and 1000 ms (black) for models W15-4 (top), L15-3 (middle), and N20-3 (bottom), respectively.

amplitude turbulent flow in and below the neutrinospheric region. When strong convection inside the PNS is encountered for $t \gtrsim 0.8$ s the spectrogram drastically changes, being dominated by angular modes with $l = 4$, but still with $C_l^{\max} \sim 10^{-4}$. The electron neutrino flux density variations rise somewhat to a level of 10% to 20%, and become manifest in the total energy loss rate, too (Figs. 4, 5).

Model N20-2 exhibits quite a similar behavior as model W15-4 except for the appearance of even larger ($l \sim 3$) angular structures clearly recognizable in the pseudo-power spectrogram between 1.0 s and 1.2 s (Figs. 7, 8). This differs from the behavior of model L15-3, where the amplitudes and angular size of the energy flux density variations remain small and even decrease in the post-explosion phase (Figs. 5, 7).

The reason for the fluctuation behavior of the neutrino emission during the vigorous pre-explosion and post-explosion accretion phases has been discussed, but what causes the spatial and temporal variations during the post-accretion phase? As the explosion is well on its way then, neither post-shock convection nor the SASI nor accretion can be responsible. Hence,

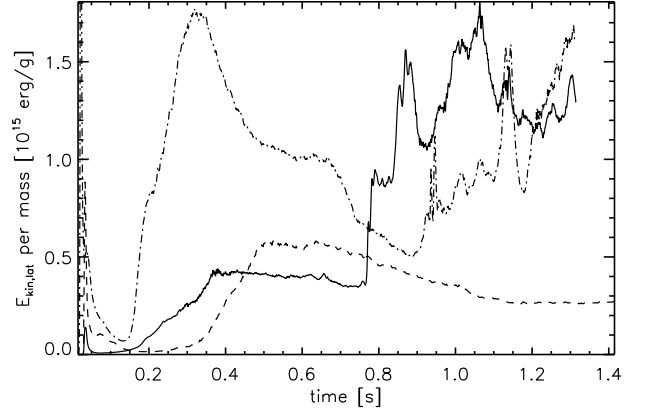


Fig. 9. Evolution of the non-radial specific kinetic energy $(v_\theta^2 + v_\phi^2)/2$ volume averaged over the computational domain inside the neutrinosphere for models W15-4 (solid), L15-3 (dashed), and N20-2 (dashed-dotted), respectively.

there only remains non-radial gas flow in the outer layers of the proto-neutron star. Ledoux convection in the proto-neutron star thus may eventually become visible, *i.e.*, its presence in the inner parts of the computational domain may become dominant in observable signals. This happens in models W15-4 and N20-2, where the level of the non-radial specific kinetic energy $(v_\theta^2 + v_\phi^2)/2$, volume averaged over the computational domain, inside the neutrinosphere shows a steep rise at ~ 0.8 s and ~ 0.9 s, respectively (Fig. 9). These non-radial flows that develop in models W15-4 and N20-2 at late times also become manifest in all discussed quantities: $\Lambda_{\max}(\Omega, t)$, $\Lambda_{\min}(\Omega, t)$, C_l^{\max} , the dominant low l -modes ($2 \lesssim l \lesssim 4$), and relative angular flux-density variations. In contrast, no such effect is present in model L15-3 (see Fig. 9), where we find a steady decrease of $\Lambda_{\max}(\Omega, t) - \Lambda_{\min}(\Omega, t)$, higher l -modes ($l \gtrsim 10$), smaller C_l^{\max} , and lower flux-density variation amplitudes than in models W15-4 and N20-2 (see Figs. 4, 5, and 7).

Simulations with fully self-consistent treatment of the PNS interior show the presence of convection inside the PNS, *i.e.*, below the neutrinosphere (see Keil et al (1996); Buras et al. (2006); Dessart et al. (2006)) more or less from the early post-bounce phase on. With the use of our inner radial grid boundary excising the inner parts of the PNS, and imposing neutrino luminosities at this boundary, convective activity is triggered only when the neutrino energy (or lepton number) inflow into the layers close to the grid boundary is faster than neutrino transport can carry away this energy (or lepton number). Then convectively unstable gradients develop and convective flows begin to carry the energy and lepton-number outwards. Whether this happens or not depends on the boundary luminosities as well as on the location of the grid boundary within the density and temperature profiles of the PNS layers below the neutrinosphere. That location determines the efficiency of the neutrino transport and varies with the stellar progenitor, whose mass-infall rate decides about how much mass accumulates in the near-surface layers of the PNS outside the inner grid boundary. The relative strength of the artificially imposed inflow of neutrino energy and lepton number compared to the efficiency of the neutrino transport on the grid, both sensitive to the location and contraction of the grid boundary on the one hand and the chosen values of the boundary luminosities on the other, therefore decides about when, where, and how strongly convective activity develops below the neutrinosphere.

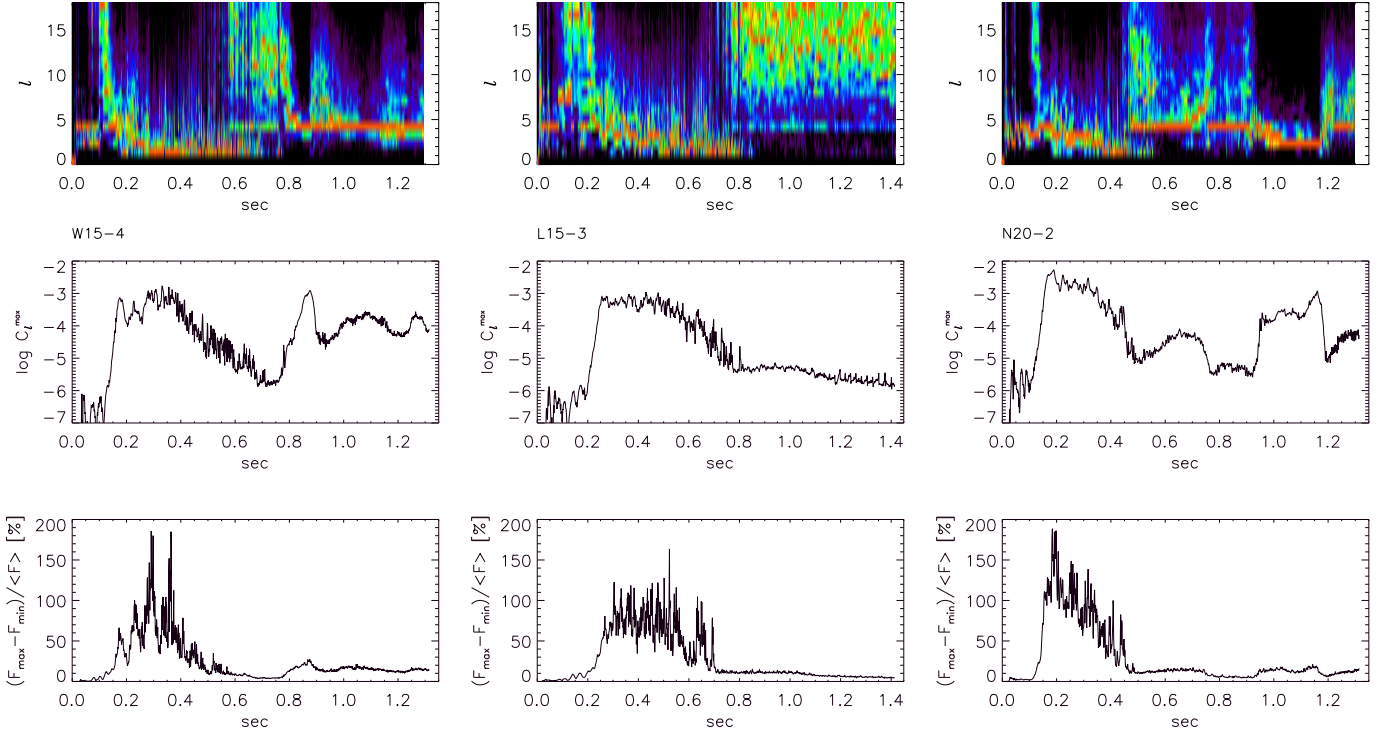


Fig. 7. Pseudo-power spectrogram of the electron-neutrino energy flux density (top row) for models W15-4 (left), L15-3 (middle), and N20-2 (right), respectively. The panels in the middle row show the corresponding maximum pseudo-power coefficient C_l^{\max} as a function of time, and the panels in the lower row give the relative angular variation of the electron neutrino flux density (maximum minus minimum flux density on the sphere divided by the angle-averaged flux density in percent) with time.

As the position of and the conditions imposed at the inner boundary can thus influence the neutrino emission properties, in particular during the post-accretion phase, our respective model predictions must be considered with care. While they do not allow to make any definite statements concerning the neutrino signal of a particular progenitor model due to the neglected treatment of the inner parts of the proto-neutron star, the models nevertheless show that convective flows below the neutrinosphere are likely to imprint themselves on the neutrino emission, and hence also on the GW signal of core collapse supernovae. A measurement of these signals may actually provide some insight in the conditions inside proto-neutron stars.

As the neutrino energy flux density varies in our models both with latitude and longitude, the observable neutrino luminosity $L_o(t)$ is obtained by an integral over the hemisphere visible to an observer (Eq. 10). In Fig. 10 we show for one chosen viewing direction the observable electron neutrino and electron antineutrino luminosities for the three models W15-4, L15-3, and N20-2, respectively. The results for other directions look very similar with all characteristic features being independent of the observer position. We provide these quantities in addition to the total neutrino energy loss rate (Eqs. 13 and 15; Figs. 4 and 5), as their temporal evolutions are the ones expected to be measurable in the IceCube and Super-Kamiokande detectors. These detectors (mainly for $\bar{\nu}_e$) will be sensitive to a combination of the observable neutrino luminosity L_o and the observable mean neutrino energy $\langle E \rangle_o$. Thus, we also provide in Fig. 10 the time evolution of the observable mean neutrino energy and of the combination $L_o \langle E \rangle_o^2$, which (roughly) enters the IceCube detection rate of Cherenkov photons originating from the dominant inverse beta decay reaction $\bar{\nu}_e + p \rightarrow n + e^+$ (Lund et al. 2010).

¹ Again one can recognize the different evolution stages, and in particular the post-shock convection and SASI phase, during which the quantity $L_o \langle E \rangle_o^2$ exhibits rapid small-amplitude variations for all three models. The level of the variations is a few percent (Fig. 10), and thus considerably smaller than that of the angular fluctuation amplitudes of the flux density, which reaches almost 100% for the total neutrino flux density (Fig. 6) and almost 200% for the electron neutrino and electron antineutrino flux densities (Fig. 7, lower panels). However, as the flux density variations are due to a few individual hot spots covering only angular areas of size $\sim (\pi/9)^2$, the observable fluctuations (of L_o and $\langle E \rangle_o$) are smaller by a factor of roughly $(\pi/9)^2 / (2\pi) \sim 1/50$. Some of such activity is also present at late times in the two models W15-4 and N20-2, where Ledoux convection develops in the simulated outer parts of the proto-neutron star (see discussion above).

From the results presented above we conclude that the signals carry clear information about the postshock hydrodynamic activity, and about the duration and decay of the accretion period. Also composition-shell interfaces present in the progenitor star can have an imprint. In model W15-4 the transition from the Fe-core to the Si-shell manifests itself in fast drops of the luminosities of ν_e and $\bar{\nu}_e$ at ~ 150 msec, when the mass accretion rate decreases steeply at the time the interface between the Fe-core and the Si-shell of the $15 M_\odot$ progenitor falls through the shock.

¹ Note that our transport approximation only provides luminosities and mean energies, but not the higher moments of the energy spectrum (see Sect. 3.1).

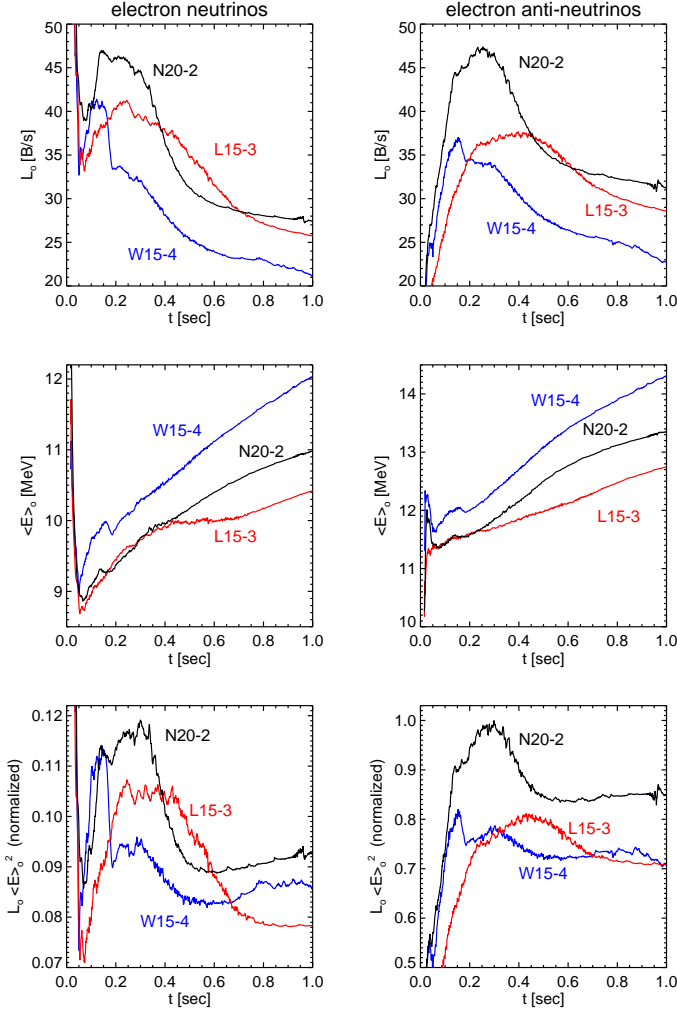


Fig. 10. Observable luminosity L_o (top row), observable mean energy $\langle E \rangle_o$ (middle row), and normalized quantity $L_o \langle E \rangle_o^{-2}$ (bottom row) of electron neutrinos (left column) and electron anti-neutrinos (right column) as a function of time for three of our models. Although we only present the results for one particular observer direction here, the global behavior and characteristics are very similar for all viewing directions.

4. Gravitational wave signature

Non-radial mass motions due to gravity waves in the near-surface layers of the PNS, which are caused by the SASI and convection in the post-shock region as well as by convective activity inside the proto-neutron star (Murphy et al. 2009; Marek et al. 2009) (driven by Ledoux unstable lepton or entropy gradients) result into a time-dependent, aspherical density stratification which produces gravitational radiation. The anisotropic emission of neutrinos associated with the non-radial mass flow (see Sect. 3) contributes to the gravitational wave signal, too. We computed and analyzed the signature of this gravitational radiation for the 3D models discussed in Sect. 2.3.

4.1. Formalism

4.1.1. Non-radial mass flow

If a source is of genuine three-dimensional nature, as it is the case for our models, it is common to express the gravitational

quadrupole radiation tensor, \mathbf{h}^{TT} , in the transverse traceless gauge in the following tensorial form

$$\mathbf{h}^{\text{TT}}(\mathbf{X}, t) = \frac{1}{R} (A_+ \mathbf{e}_+ + A_\times \mathbf{e}_\times) \quad (19)$$

(see, e.g., Misner et al. (1993)). R denotes the distance between the observer and the source, and the unit linear-polarization tensors are given by

$$\mathbf{e}_+ = \mathbf{e}_\theta \otimes \mathbf{e}_\theta - \mathbf{e}_\phi \otimes \mathbf{e}_\phi, \quad (20)$$

$$\mathbf{e}_\times = \mathbf{e}_\theta \otimes \mathbf{e}_\phi + \mathbf{e}_\phi \otimes \mathbf{e}_\theta, \quad (21)$$

with \mathbf{e}_θ and \mathbf{e}_ϕ being the unit polarization vectors in θ and ϕ -direction of a spherical coordinate system, and \otimes denoting the tensor product.

The wave amplitudes A_+ and A_\times represent the only two independent modes of polarization in the TT gauge (Misner et al. 1993). In the slow-motion limit, they are obtained from linear combinations of the second time derivatives (evaluated at retarded time, and denoted by a double dot accent) of the components of the transverse traceless mass quadrupole tensor (Misner et al. 1993)

$$A_+ = \ddot{Q}_{\theta\theta} - \ddot{Q}_{\phi\phi}, \quad (22)$$

$$A_\times = 2\ddot{Q}_{\theta\phi}. \quad (23)$$

We computed the latter using a post-Newtonian approach whereby the numerically troublesome second order time derivatives of the mass quadrupole tensor components are transformed into much better tractable spatial derivatives. Following Nakamura & Oohara (1989) and Blanchet, Damour & Schäfer (1990) the second time derivatives read in a Cartesian orthonormal basis (the spatial indices i and j run from 1 to 3)

$$\ddot{Q}_{ij} = \frac{G}{c^4} \int d^3x \rho \left(2v_i v_j - x_i \partial_j \Phi_{\text{eff}} - x_j \partial_i \Phi_{\text{eff}} \right), \quad (24)$$

where G is Newton's gravitational constant, c the speed of light in vacuum, Φ_{eff} the effective Newtonian gravitational potential including the general relativistic ‘‘case A’’ correction of the monopole term due to Marek et al. (2006), ρ the mass-density, v_i the Cartesian velocity components, and ∂_i the partial derivative with respect to the coordinate x^i of a Cartesian basis.

We note that the integrand in Eq. (24) has compact support and is known to the (2nd order) accuracy level of the numerical scheme employed in the hydrodynamics code. It can easily be shown that evaluating the integral of Eq. (24) by an integration scheme (of at least 2nd order) is by one order of accuracy superior to twice applying numerical time-differentiation methods to quadrupole data given at discrete points of time (Finn & Evans 1990; Mönchmeyer et al. 1991).

Exploiting the coordinate transformation between the orthonormal Cartesian basis x^i and the orthonormal basis in spherical coordinates \hat{x}^i (with $\hat{x}^i \in [r, \theta, \phi]$), the wave amplitudes A_+ and A_\times (Eqs. (22) & (23)) are obtained from the following second time derivatives of the spherical components of the mass quadrupole tensor (Oohara et al. 1997; Scheidegger et al. 2008)

$$I_{\theta\theta}^{\text{TT}} = \left(I_{xx}^{\text{TT}} \cos^2 \phi + I_{yy}^{\text{TT}} \sin^2 \phi + 2 I_{zz}^{\text{TT}} \sin \phi \cos \phi \right) \cos^2 \theta + I_{yy}^{\text{TT}} \sin^2 \theta - 2 \left(I_{xz}^{\text{TT}} \cos \phi + I_{yz}^{\text{TT}} \sin \phi \right) \sin \theta \cos \theta, \quad (25)$$

$$I_{\phi\phi}^{\text{TT}} = I_{xx}^{\text{TT}} \sin^2 \phi + I_{yy}^{\text{TT}} \cos^2 \phi - 2 I_{xy}^{\text{TT}} \sin \phi \cos \phi, \quad (26)$$

$$I_{\theta\phi}^{\text{TT}} = \left(I_{yy}^{\text{TT}} - I_{xx}^{\text{TT}} \right) \cos \theta \sin \phi \cos \phi + I_{xy}^{\text{TT}} \cos \theta \left(\cos^2 \phi - \sin^2 \phi \right) + I_{xz}^{\text{TT}} \sin \theta \sin \phi - I_{yz}^{\text{TT}} \sin \theta \cos \phi, \quad (27)$$

where we used the abbreviation

$$I_{ij}^{TT} \equiv \ddot{Q}_{ij}^{TT}. \quad (28)$$

Choosing $\phi = 0$ one obtains the polarization modes (see, e.g., Misner et al. (1993))

$$A_+ = I_{xx}^{TT} - I_{yy}^{TT}, \quad (29)$$

$$A_\times = 2I_{xy}^{TT}, \quad (30)$$

for $\theta = 0$, and

$$A_+ = I_{zz}^{TT} - I_{yy}^{TT}, \quad (31)$$

$$A_\times = -2I_{yz}^{TT}, \quad (32)$$

for $\theta = \pi/2$, respectively. These expressions were already discussed in earlier investigations concerned with the evaluation of the gravitational wave signature of 3D core collapse supernova models (Müller & Janka 1997; Fryer et al. 2004; Scheidegger et al. 2008, 2010).

The total energy radiated in the form of gravitational waves due to nonspherical mass flow is given in the quadrupole approximation by (see, e.g., Misner et al. (1993))

$$\begin{aligned} E_M &= \frac{c^3}{5G} \int_0^\infty \sum_{ij} \left[\frac{d}{dt} \left(I_{ij}^{TT} - \frac{1}{3} \delta_{ij} \sum_l I_{ll}^{TT} \right) \right]^2 dt \\ &= \frac{c^3}{15G} \int_0^\infty dt \left[(i_{xx}^{TT} - i_{yy}^{TT})^2 + (i_{xx}^{TT} - i_{zz}^{TT})^2 \right. \\ &\quad \left. + (i_{yy}^{TT} - i_{zz}^{TT})^2 + 6 \left((i_{xy}^{TT})^2 + (i_{xz}^{TT})^2 + (i_{yz}^{TT})^2 \right) \right], \end{aligned} \quad (33)$$

with $i_{ij}^{TT} \equiv \partial I_{ij}^{TT} / \partial t$, and the corresponding GW spectral energy density is given by (where ν denotes the frequency)

$$\begin{aligned} \frac{dE_M}{d\nu} &= \frac{2c^3}{15G} (2\pi\nu)^2 \left[|\tilde{I}_{xx}^{TT} - \tilde{I}_{yy}^{TT}|^2 + |\tilde{I}_{xx}^{TT} - \tilde{I}_{zz}^{TT}|^2 \right. \\ &\quad \left. + |\tilde{I}_{yy}^{TT} - \tilde{I}_{zz}^{TT}|^2 + 6 \left(|\tilde{I}_{xy}^{TT}|^2 + |\tilde{I}_{xz}^{TT}|^2 + |\tilde{I}_{yz}^{TT}|^2 \right) \right], \end{aligned} \quad (34)$$

where

$$\tilde{I}_{ij}^{TT}(\nu) = \int_{-\infty}^{\infty} I_{ij}^{TT}(t) e^{-2\pi i \nu t} dt \quad (35)$$

is the Fourier transform of $I_{ij}^{TT}(t)$.

4.1.2. Anisotropic neutrino emission

To determine the gravitational wave signal associated with the anisotropic emission of neutrinos, we follow Müller & Janka (1997) and use Eq. (16) of Epstein (1978) in the limit of a distant source, $R \rightarrow \infty$, together with the approximation that the gravitational wave signal measured by an observer at time t is caused only by radiation emitted at time $t' = t - R/c$. Hence, we take $t - t' = \text{const} = R/c$, i.e., we assume that only the neutrino pulse itself causes a gravitational wave signal, whereas memory effects, which prevail after the pulse has passed the observer, are disregarded.

With these simplifications, the dimensionless gravitational wave amplitudes of the two polarisation modes are given in the transverse-traceless gauge for an observer located at a distance R along the z -axis of the observer frame by Müller & Janka (1997)

$$h_+(t) = \frac{2G}{c^4 R} \int_0^t dt' \int_{4\pi} d\Omega' (1 + \cos \theta) \cos 2\phi \frac{d\Lambda(\Omega', t')}{d\Omega'} \quad (36)$$

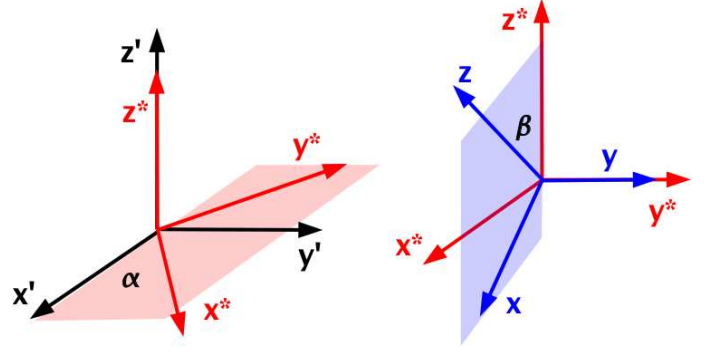


Fig. 11. Relation between the source coordinate system (x', y', z') and the observer coordinate system (x, y, z) . Changing from the observer system to the source system involves a rotation by an angle α about the z' -axis to an intermediate coordinate system (x^*, y^*, z^*) , followed by a rotation by an angle β about the y^* -axis (which thus is also the y -axis).

and

$$h_\times(t) = \frac{2G}{c^4 R} \int_0^t dt' \int_{4\pi} d\Omega' (1 + \cos \theta) \sin 2\phi \frac{d\Lambda(\Omega', t')}{d\Omega'}, \quad (37)$$

respectively. Here $d\Lambda(\Omega', t')/d\Omega'$ is given by Eq. (12) and denotes the total neutrino energy radiated at time t' per unit of time into a solid angle $d\Omega'$ in direction (θ', ϕ') . Except for position dependent factors the gravitational wave amplitudes are simply a function of this quantity provided by the ray-by-ray transport approximation (note that in Müller & Janka (1997) we used the symbol L_ν instead of Λ).

The angular integration, $d\Omega' = -d(\cos \theta') d\phi'$, in Eqs. (36) and (37) extends over all angles θ' and ϕ' in the coordinate frame of the source (x', y', z') that we identify with the (arbitrarily chosen) spherical polar coordinate frame to which the hydrodynamic results were mapped from the Yin-Yang grid employed in the simulations. For the evaluation of the polarisation modes we used the (asymptotic) values of $d\Lambda(\Omega, t)/d\Omega$ extracted at a radius of 500 km from our 3D models.

The angles θ and ϕ in Eqs. (36) and (37) are measured in the observer frame (x, y, z) , while the neutrino luminosity is measured in the source frame (x', y', z') . To allow for an arbitrary orientation of the observer relative to the source, we introduce two viewing angles $\alpha \in [-\pi, +\pi]$ and $\beta \in [0, \pi]$ (see Fig. 11). The coordinates measured in the observer frame are then related to the coordinates in the source frame by the following coordinate transformations

$$x^* = x' \cos \alpha + y' \sin \alpha, \quad (38)$$

$$y^* = -x' \sin \alpha + y' \cos \alpha, \quad (39)$$

$$z^* = z', \quad (40)$$

and

$$x = x^* \cos \beta - z^* \sin \beta, \quad (41)$$

$$y = y^*, \quad (42)$$

$$z = x^* \sin \beta + z^* \cos \beta. \quad (43)$$

With these coordinate transformations and the relations

$$x = r \sin \theta \cos \phi, \quad (44)$$

$$y = r \sin \theta \sin \phi, \quad (45)$$

$$z = r \cos \theta \quad (46)$$

between Cartesian coordinates (x, y, z) and spherical polar coordinates (r, θ, ϕ) , we obtain

$$\sin \theta \cos \phi = (\cos \phi' \cos \alpha + \sin \phi' \sin \alpha) \sin \theta' \cos \beta - \cos \theta' \sin \beta, \quad (47)$$

$$\sin \theta \sin \phi = (\sin \phi' \cos \alpha - \cos \phi' \sin \alpha) \sin \theta', \quad (48)$$

$$\cos \theta = (\cos \phi' \cos \alpha + \sin \phi' \sin \alpha) \sin \theta' \sin \beta + \cos \theta' \cos \beta. \quad (49)$$

These expressions relate the angular coordinates in the observer frame (θ, ϕ) to those in the source frame (θ', ϕ') . For the special case $\alpha = 0$ they were already presented by Kotake et al. (2009a). Using Eq. (49) and the equalities

$$\sin 2\phi = \frac{2xy}{x^2 + y^2}, \quad (50)$$

$$\cos 2\phi = \frac{x^2 - y^2}{x^2 + y^2} \quad (51)$$

derived from Eqs. (44) to (46), the two polarization modes (Eqs. 36 and 37) are given by

$$h_S(t, \alpha, \beta) = \frac{2G}{c^4 R} \int_0^t dt' \Lambda(t') \alpha_S(t', \alpha, \beta), \quad (52)$$

where $S \in (+, \times)$ and $\Lambda(t)$ is the angular integral of the neutrino energy radiated at time t per unit of time given in Eqs. (13) and (15).

$$\alpha_S(t, \alpha, \beta) = \frac{1}{\Lambda(t)} \int_{4\pi} d\Omega' W_S(\Omega', \alpha, \beta) \frac{d\Lambda(\Omega', t)}{d\Omega'}, \quad (53)$$

are anisotropy parameters, which provide a quantitative measure of the time-dependent anisotropy of the emission in both polarization modes. Note that the evaluation of the anisotropy parameter $\alpha(t)$ defined in Eq. (29) of Müller & Janka (1997), which should not be confused with the observer angle α introduced in Fig. 11, does neither involve a dependence on observer angles (α, β) nor on the polarization mode.

The angular weight functions appearing in the above expression for the anisotropy parameters are given by

$$W_S(\theta', \phi', \alpha, \beta) = \frac{D_S(\theta', \phi', \alpha, \beta)}{N(\theta', \phi', \alpha, \beta)}, \quad (54)$$

where

$$D_+ = [1 + (\cos \phi' \cos \alpha + \sin \phi' \sin \alpha) \sin \theta' \sin \beta + \cos \theta' \cos \beta] \{[(\cos \phi' \cos \alpha + \sin \phi' \sin \alpha) \sin \theta' \cos \beta - \cos \theta' \sin \beta]^2 - \sin^2 \theta' (\sin \phi' \cos \alpha - \cos \phi' \sin \alpha)^2\}, \quad (55)$$

$$D_\times = [1 + (\cos \phi' \cos \alpha + \sin \phi' \sin \alpha) \sin \theta' \sin \beta + \cos \theta' \cos \beta] 2 [(\cos \phi' \cos \alpha + \sin \phi' \sin \alpha) \sin \theta' \cos \beta - \cos \theta' \sin \beta] \sin \theta' (\sin \phi' \cos \alpha - \cos \phi' \sin \alpha), \quad (56)$$

$$N = [(\cos \phi' \cos \alpha + \sin \phi' \sin \alpha) \sin \theta' \cos \beta - \cos \theta' \sin \beta]^2 + \sin^2 \theta' (\sin \phi' \cos \alpha - \cos \phi' \sin \alpha)^2. \quad (57)$$

Choosing $\alpha = 0$ and $\beta = \pi/2$ the observer is located in the equatorial plane of the source (*i.e.*, perpendicular to the source's z' -axis) at the azimuthal position $\phi' = 0$. In that case one obtains simpler expressions for the angular functions (see also Kotake et al. (2009a))

$$W_{+|e} = (\cos^2 \theta' - \sin^2 \theta' \sin^2 \phi') \frac{1 + \sin \theta' \cos \phi'}{\cos^2 \theta' + \sin^2 \theta' \sin^2 \phi'}, \quad (58)$$

$$W_{\times|e} = -2 \cos \theta' \sin \theta' \sin \phi' \frac{1 + \sin \theta' \cos \phi'}{\cos^2 \theta' + \sin^2 \theta' \sin^2 \phi'}. \quad (59)$$

Note that for axisymmetric sources $h_\times = 0$.

In general, the total energy $E_{\text{GW}}(t)$ radiated to infinity by a source in form of gravitational waves until time t is given by (see, *e.g.*, Misner et al. (1993); Greek indices run from 0 to 3, and repeated indices are summed over)

$$E_{\text{GW}}(t) = \int_0^t dt' \int_{S_\infty^2} \tau_{0\nu} n^\nu r^2 d\Omega, \quad (60)$$

where the angular integration is performed over a two-sphere at spatial infinity S_∞^2 , and $n^\mu = (0, 1, 0, 0)$ is a unit spacelike vector in polar coordinates $\{ct, r, \theta, \phi\}$ normal to S_∞^2 . Denoting by $\langle \dots \rangle$ an average over several wavelengths, the gravitational-wave energy-momentum tensor $\tau_{\mu\nu}$ is given in transverse-traceless gauge by

$$\tau_{\mu\nu} = \frac{c^5}{32\pi G} \langle (\partial_\mu h_{\text{TT}}^{\rho\sigma}) (\partial_\nu h_{\text{TT}}^{\rho\sigma}) \rangle. \quad (61)$$

Thus, Eq. (60) can be rewritten as

$$E_{\text{GW}}(t) = \frac{c^3}{32\pi G} \int_0^t dt' \int_{S_\infty^2} r^2 d\Omega \langle (\partial_t h_{ik}^{\text{TT}}) (\partial_r h_{ik}^{\text{TT}}) \rangle, \quad (62)$$

where we have used the facts that $h_{0r}^{\text{TT}} = 0$, $h_{lr}^{\text{TT}} = 0$, and $c \partial_r h_{ik}^{\text{TT}} = -\partial_t h_{ik}^{\text{TT}}$ for radially outgoing gravitational radiation. Evaluating the double sum in Eq. (62) and using the relations $h_{\theta\theta}^{\text{TT}} = -h_{\phi\phi}^{\text{TT}} = h_+$ and $h_{\theta\phi}^{\text{TT}} = h_{\phi\theta}^{\text{TT}} = h_\times$ (see, *e.g.*, Misner et al. (1993)), we finally find

$$E_{\text{GW}}(t) = \frac{c^3}{16\pi G} \int_0^t dt' \int_{S_\infty^2} r^2 d\Omega \langle (\partial_t h_+)^2 + (\partial_t h_\times)^2 \rangle. \quad (63)$$

Inserting the expressions for h_+ and h_\times given in Eq. (52) into Eq. (63) we obtain for the energy $E_N(t)$ radiated in form of gravitational waves until time t due to anisotropic neutrino emission

$$E_N(t) = \frac{G}{4\pi c^5} \int_0^t dt' \int_{4\pi} d\Omega_{\alpha\beta} [l_+^2(t', \alpha, \beta) + l_\times^2(t', \alpha, \beta)] \quad (64)$$

with $d\Omega_{\alpha\beta} = \sin \beta d\beta d\alpha$ and

$$l_S(t, \alpha, \beta) = \Lambda(t) \alpha_S(t, \alpha, \beta). \quad (65)$$

The corresponding spectral energy density is given by

$$\frac{dE_N}{d\nu} = \frac{G}{2\pi c^5} |\tilde{l}(\nu)|^2, \quad (66)$$

where $\tilde{l}(\nu)$ is the Fourier transform of

$$l(t) = \left\{ \int_{4\pi} d\Omega_{\alpha\beta} [l_+^2(t, \alpha, \beta) + l_\times^2(t, \alpha, \beta)] \right\}^{1/2}. \quad (67)$$

For completeness we also provide an expression for the total energy radiated in form of gravitational waves until time t , *i.e.*, due to anisotropic mass flow **and** neutrino emission. It is obtained by inserting the total GW amplitude, *i.e.*, the sum of the amplitudes given by Eqs. (19) and (52) into Eq. (63), which leads to

$$E_{\text{GW}} = \frac{c^3}{16\pi G} \int_0^t dt' \int_{4\pi} d\Omega \left[\left(\frac{2G}{c^4} l_+ + \partial_t A_+ \right)^2 + \left(\frac{2G}{c^4} l_\times + \partial_t A_\times \right)^2 \right]. \quad (68)$$

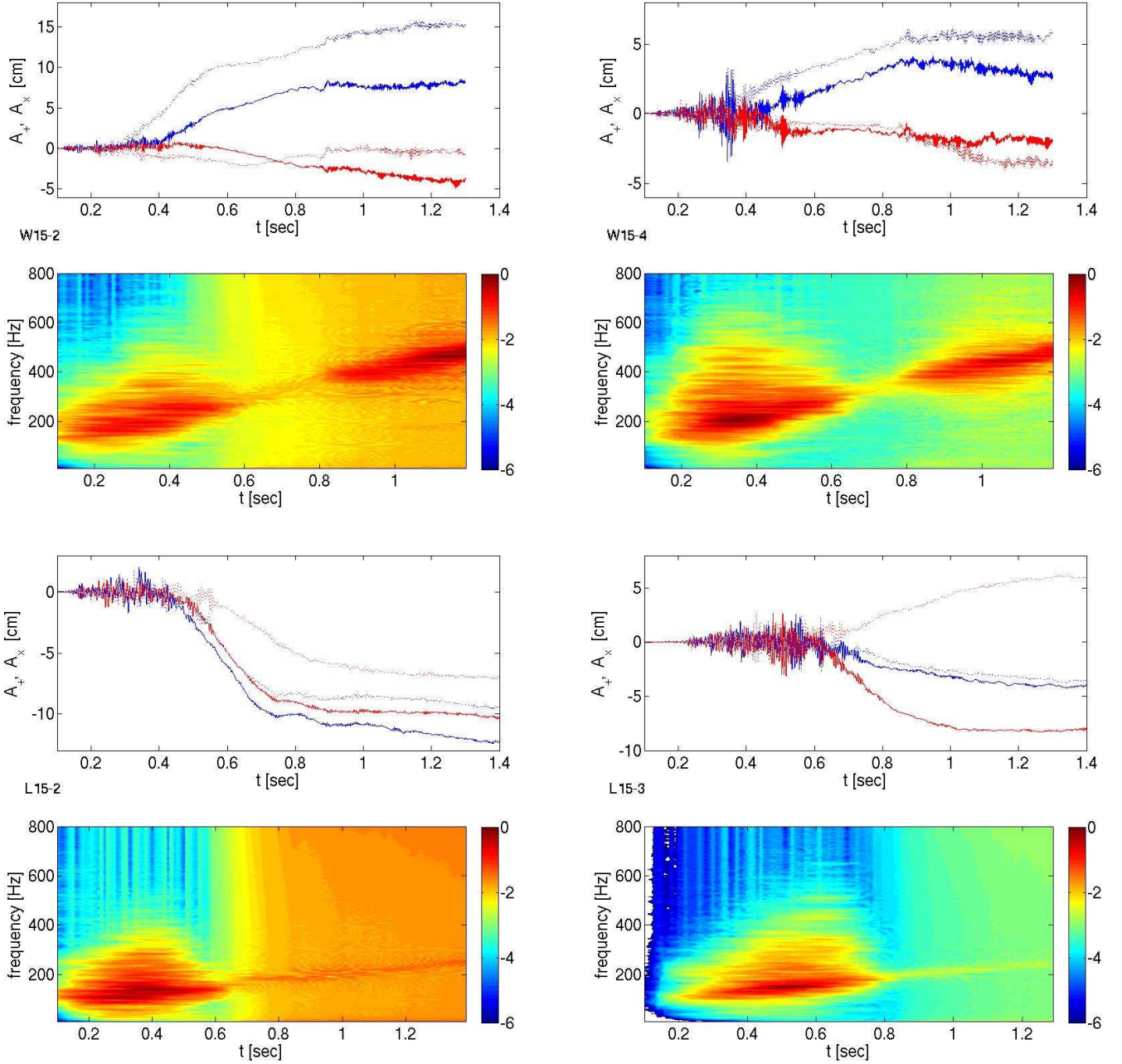


Fig. 12. The four panels show the gravitational wave amplitudes (top) and spectrograms of $dE_M/d\nu$ (bottom; normalized to the absolute maximum) arising from non-spherical mass flow of models W15-2 (top left), W15-4 (top right), L15-2 (bottom left), and L15-3 (bottom right), respectively. Blue curves give the amplitude A_+ at the pole (solid) and the equator (dotted), while red curves show the other independent mode of polarization A_\times from the same directions.

4.2. Results

Although an observer can only measure the total gravitational wave amplitude, *i.e.*, that due to the combined effect of non-radial flow and anisotropic neutrino emission, we will first discuss the GW signal of non-radial mass flow only, because it reflects the various phases of the post-bounce evolution already introduced in the discussion of the neutrino signal above.

Until post-shock convection and the SASI are eventually mature at around 150 msec, the GW signal is very small (Fig. 12).²

² Note that our models, because of the excised inner region of the PNS, are not able to follow the GW emission due to prompt post-shock convection (see Marek et al. (2009)).

Later on, sizable g-mode activity is instigated in the outer layers of the proto-neutron star by convective overturn and the SASI during the hydrodynamically vigorous pre-explosion phase, and by the impact of anisotropic accretion flows during the subsequent post-explosion accretion phase (Marek et al. 2009). This g-mode activity is the cause of GW signals (Marek et al. 2009; Murphy et al. 2009; Yakunin et al. 2010), whose maximum amplitudes are of the order of a few centimeters centered around zero.

The GW frequency distribution possesses a very broad maximum in the range of 100 Hz to 500 Hz, and the frequency corresponding to this maximum slowly increases with time (Fig. 12). Partially already during the post-explosion accretion phase, but

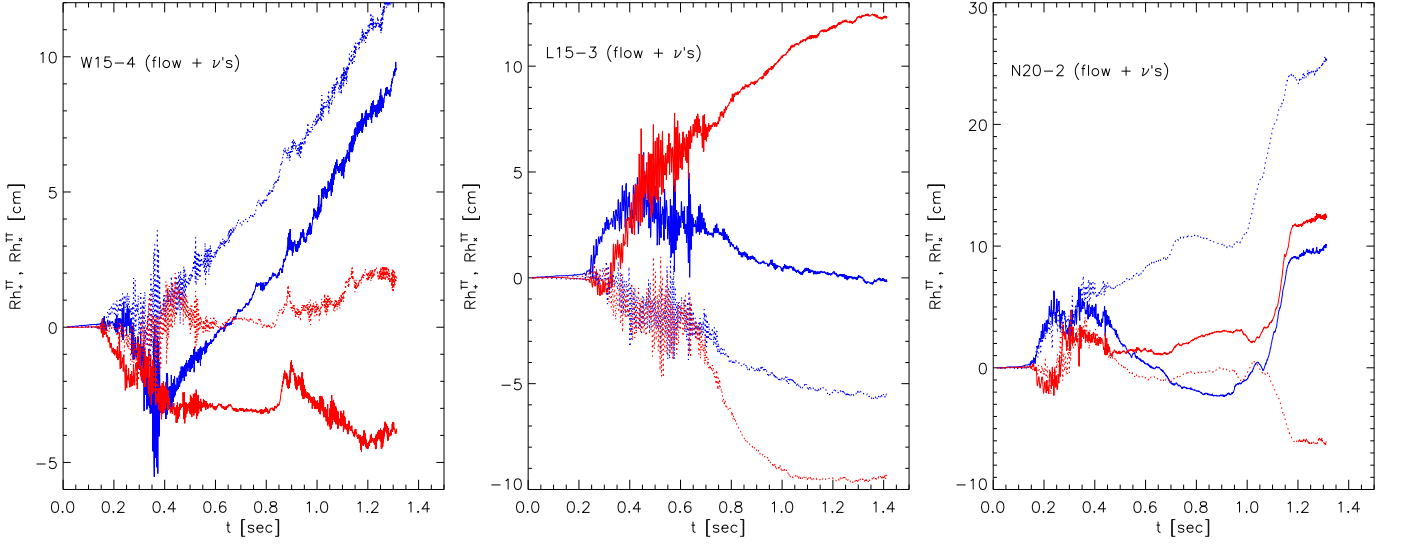


Fig. 13. Gravitational wave amplitudes Rh_+^{TT} (blue) and Rh_x^{TT} (red) due to anisotropic mass flow and neutrino emission as a function of time for models W15-4 (left), L15-3 (middle), and N20-3 (right), respectively. The solid curves show the amplitudes for an observer located above the north pole ($\alpha = \beta = 0$; see Fig. 11) of the source, while the other curves give the amplitudes at the equator ($\alpha = 0, \beta = \pi/2$).

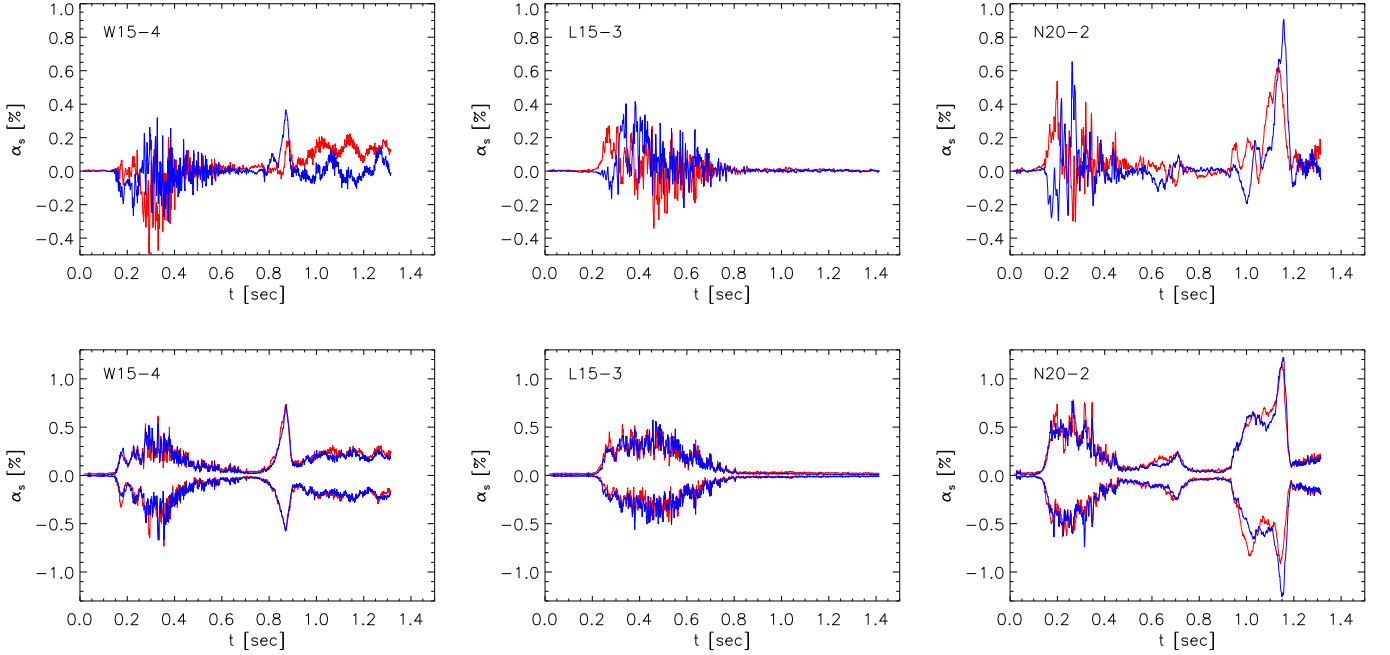


Fig. 14. Asymmetry parameter α_s of the neutrino emission (Eq. 53) as a function of time for models W15-4 (left), L15-3 (middle), and N20-2 (right), respectively. The panels in the upper row show α_+ (blue) and α_x (red) for a particular observer direction, while the panels in the lower row give for both parameters the maximum and minimum values in all directions.

latest when the shock wave starts rapidly propagating to large radii between ~ 0.4 sec and ~ 0.7 sec (see Figs. 4 and 5), the GW amplitudes start to grow by about a factor of ten until approximately asymptoting at ~ 0.9 sec in the case of the models based on the progenitor W15, and at ~ 1 sec in the case of models based on the progenitor L15, respectively (Fig. 12). This growth of the amplitude is associated with the anisotropic expansion of the shock wave and a positive/negative wave amplitude indicates a prolate/oblate explosion, respectively (Murphy et al. 2009).

While the GW amplitudes grow the GW energy distribution $dE_M/d\nu$ becomes much narrower and dimmer, and the fre-

quency at maximum power continues to increase. The latter effect was also observed in the 2D models of Murphy et al. (2009). At late times, the GW signal of the W15 models clearly signifies the convective activity inside the proto-neutron star through small amplitude, high frequency fluctuations around the asymptotically roughly constant mean GW amplitudes, while no such fluctuations are present in the case of the L15 models (see discussion of the neutrino signal above). This model discrepancy is also evident from the energy spectrograms, which do exhibit a pronounced broad maximum (between ~ 350 Hz and ~ 550 Hz) at $t > 0.8$ sec in the case of the W15 models, but none for the L15

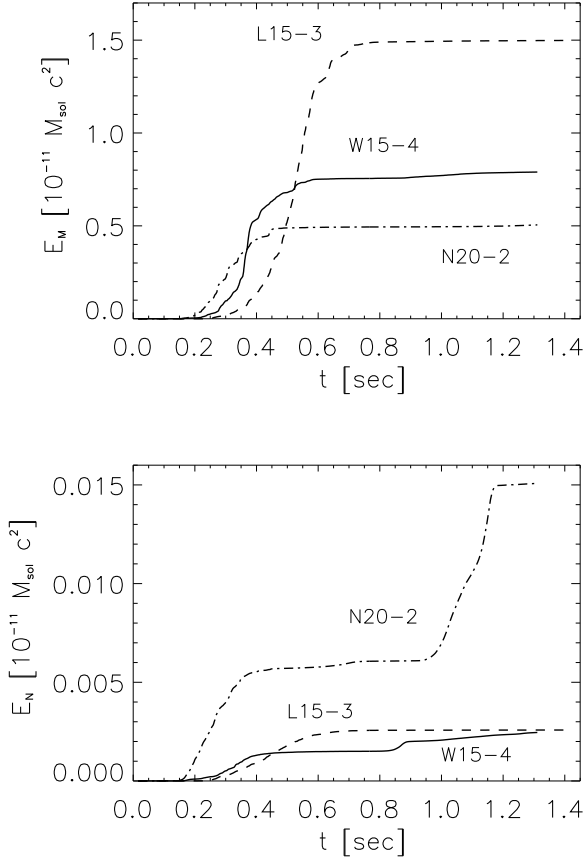


Fig. 15. Energy emitted in form of gravitational waves due to anisotropic mass flow (top panel) and due to anisotropic neutrino emission (bottom panel) as a function of time for models W15-4 (solid), L15-3 (dashed), and N20-2 (dash-dotted), respectively.

ones. Further note that until the end of the simulations the frequency of the maximum of $dE_M/d\nu$ has increased from around 100 Hz to almost 500 Hz for the former models (due to the increasing speeds of mass motions in the postshock region at times $\lesssim 0.5$ sec and because of the increased compactness of the proto-neutron star at times $\gtrsim 0.6$ sec, respectively).

The behavior of the total (matter plus neutrinos) GW amplitudes is significantly different from that of the flow-only GW amplitudes for models which exhibit PNS convection below the neutrinosphere, *i.e.*, for the models based on the progenitors W15 and N20. Particularly at late times, anisotropic neutrino emission causes a continuing growth of the GW amplitudes (instead of a saturation) in these models, while this is not the case for the L15 models (see Fig. 13, and compare with Fig. 12). The latter behavior is also reflected in the time evolution of the asymmetry parameter α_S (Eq. 53) of the neutrino emission (Fig. 14). The asymmetry parameter is practically zero in model L15-3 at late times, while it remains, after having temporarily grown to values beyond about 0.4 - 0.5%, at the level of $\sim 0.3\%$ until the end of the simulations in models W15-4 and N20-2.

The final GW amplitudes are up to a factor of two to three larger when taking the contribution of anisotropic neutrino emission into account, but the amount of energy radiated in the form of GWs is only insignificantly changed, being practically constant for all simulated models after the onset of the explosion (see Fig. 15). The GW energy radiated by neutrinos is small

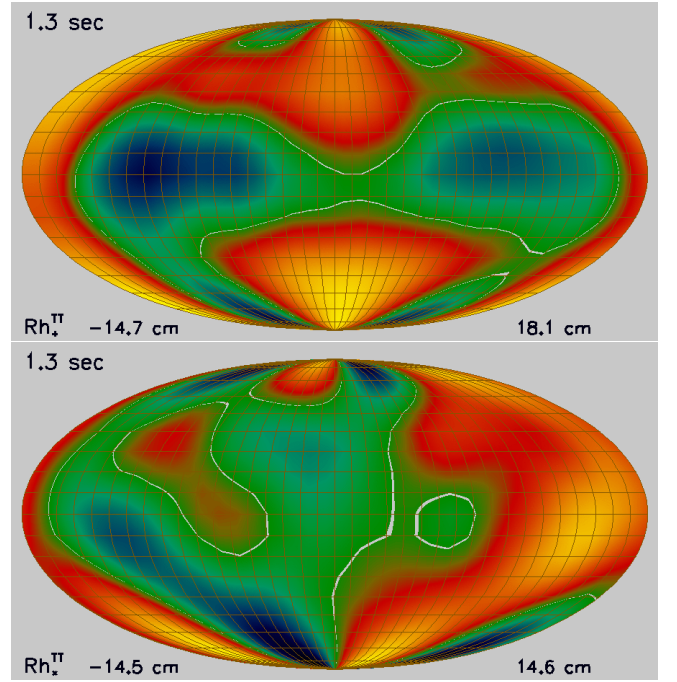


Fig. 16. Gravitational wave amplitudes due to anisotropic mass flow and neutrino emission, Rh_+^{TT} (top) and Rh_x^{TT} (bottom), as functions of the observer angles (see Fig. 11) for model W15-4 at 1.3 sec past bounce. The white contours give the locations, where the amplitudes are zero. Yellow and red areas indicate positive amplitudes, green and blue negative ones.

($\lesssim 1\%$) compared to that emitted by matter due to the slow variation of the GW neutrino amplitude with time, *i.e.*, its time derivative is much smaller than that of the GW matter amplitude. For this reason we also abstained from evaluating the total energy radiated in form of GW (Eq. 68). It differs little from that due to anisotropic matter flow alone (Eq. 33), because the mixed term in Eq. (68), resulting from the square of the sum of the matter and neutrino parts, contributes $\lesssim 10\%$ to the total radiated GW energy, and the pure neutrino term $\lesssim 1\%$. Figure 15 also shows that the (small) contribution of anisotropic neutrino emission to the radiated GW energy is enhanced at late times when proto-neutron star convection occurs below the neutrinosphere, as it is the case for models W15-4 and in particular N20-2.

The variation of the total GW amplitudes with observer angle is illustrated in Fig. 16 for model W15-4 at 1.3 sec (when the simulation was stopped). Both the amplitude variations and the typical angular size of the speckled GW emission are similar for all other simulated models. The model-independent level of the amplitude variations is also supported by Fig. 13 when comparing various amplitudes at any given (late) time.

The (normalized) amplitude spectrograms of the total gravitational wave amplitudes ($d(A_{+,x} + Rh_{+,x})/d\nu$; Figs. 17 and 18) illustrate two model-independent findings. Firstly, during the hydrodynamically vigorous pre-explosion and post-explosion accretion phases ($0.2 \lesssim t \lesssim 0.5 - 0.7$ sec) the spectra of all models are characterized by some power at low frequencies ($\lesssim 100$ Hz) and a broad power maximum at frequencies ~ 200 Hz and another weak one at ~ 800 Hz. The latter broad maximum at high frequency is more pronounced in the models based on the W15 and N20 progenitors and in the cross polarization GW mode. Secondly, during the post-accretion phase ($t \gtrsim 0.7$ sec) the spectra of all models are dominated by a low frequency

($\lesssim 40$ Hz) contribution peaked towards the lower end of the spectrogram. In the models where PNS convection occurs below the neutrinosphere (models W15 and N20) we also find a double-peaked high frequency contribution decreasing/increasing from ~ 700 Hz (400 Hz) at $t \sim 0.8$ sec, and eventually merging into a single power maximum at ~ 500 Hz at $t \sim 1.2$ sec. Again this contribution is more pronounced for the cross polarization GW mode.

The spectra of the total GW amplitudes are dominated by the contribution due to non-isotropic neutrino emission at low (≤ 100 Hz) frequencies (Figs. 17 and 18). At higher frequencies (≥ 100 Hz) the spectra of model W15-4 show two pronounced maxima (at 100 - 200 Hz and 600 - 800 Hz, respectively) at all times. These maxima are also present in model L15-3 at times ≤ 0.7 s, the high-frequency one being, however, much less pronounced. The lower maximum (at 100 - 200 Hz) results from g-mode activity in the PNS surface instigated by non-radial flow (SASI, accretion) in the post-shock region until $\sim 0.5 - 0.7$ sec. At later times PNS convection is responsible for the peak between 300 and 500 Hz. We have proposed this explanation already for the corresponding maxima present in the GW energy spectrograms arising from non-spherical mass flow (Fig. 12), and discussed why the frequencies of these maxima increase with time. The source of the high-frequency maximum (600 - 800 Hz) is unclear, but a further detailed analysis shows that (i) the maximum is solely due to non-radial gas flow, *i.e.*, it is not connected to neutrinos, (ii) it does not result from stellar layers below the neutrino sphere but from close to or slightly above it, and (iii) does not depend on the position of the observer.

Note that the high-frequency maximum present in the amplitude spectrograms is strongly suppressed in the corresponding energy spectrograms (Fig. 12), as the latter involve the squared time derivatives of the amplitudes. Thus, the already large ratio of the low and high-frequency maxima in the amplitude spectrograms (about two orders of magnitude) translates into an even larger ratio for the energy spectrogram maxima rendering the high-frequency maximum practically invisible.

5. Discussion and Conclusions

Based on a set of three-dimensional (3D) parametrized neutrino-driven supernova explosion models of non-rotating 15 and 20 M_{\odot} stars, employing a neutrino transport description with a gray spectral treatment and a ray-by-ray approximation of multi-dimensional effects (the scheme is applicable in the regime outside the dense neutron star core, *i.e.*, around and outside the neutrinosphere), we evaluated both the time-dependent and direction-dependent neutrino and gravitational-wave emission of these models. To this end we presented the formalism necessary to compute both the observable neutrino and gravitational wave signals for a genuinely three-dimensional source. For the neutrino signal we presented formulas that allow one to estimate the apparent luminosity when the local flux density on a radiating surface is known and the intensity can be assumed to be axisymmetric around the direction perpendicular to the radiating surface. For the gravitational-wave analysis we extended and generalized previous studies, where the source was either assumed to be axisymmetric or where the formulas for the signals of a 3D source were only given for special observer directions.

Our models followed the evolution from shortly after core bounce up to more than one second into the early cooling evolution of the PNS without imposing any symmetry restrictions and covering a full sphere. The extension over such a relatively long evolution time in 3D was possible through the usage of an

axis-free overset grid (the Yin-Yang grid) in spherical polar coordinates, which considerably eases the CFL time step restriction and avoids axis artifacts. A central region, the dense inner core of the proto-neutron star, was excised from the computational domain and replaced by an inner, time-dependent radial boundary condition and a gravitating point mass at the coordinate origin. Explosions in the models were initiated by neutrino heating at a rate that depends on suitably chosen values of the neutrino luminosities imposed at the inner radial boundary.

The neutrino emission properties (fluxes and effective spectral temperatures) of our 3D models exhibit the generic time-dependent features already known from 2D (axisymmetric) models (*e.g.*, Buras et al. (2006); Scheck et al. (2006); Marek et al. (2009); Brandt et al. (2011)) showing fluctuations over the neutron star surface on different spatial and temporal scales. We find that non-radial mass motions caused by the SASI and convection in the neutrino-heated hot-bubble region as well as by PNS convection below the neutrinosphere give rise to a time-dependent, anisotropic emission of neutrinos, particularly of electron neutrinos and anti-neutrinos, and thus also to the emission of gravitational waves. We have analyzed this emission, particularly addressing its anisotropy and temporal variation. We also derived apparent neutrino luminosities for an observer located at a large distance from the source. Because very prominent, quasi-periodic sloshing motions of the shock due to the standing accretion-shock instability as visible in 2D simulations are absent and the emission from different surface areas facing an observer adds up incoherently, the modulation amplitudes of the measurable neutrino luminosities and mean energies are significantly smaller than predicted by 2D models (for 2D results see Marek et al. (2009); Brandt et al. (2011)).

The post-bounce evolution of our models can be divided into four distinct phases (Fig. 4). The first phase, the *quasi-spherical shock-expansion phase*, lasts from shock formation shortly after core bounce to 80 - 150 msec, when convection sets in. The second phase, the hydrodynamically vigorous *pre-explosion phase*, comprises the growth of post-shock convection and of the standing accretion shock instability (SASI). The *post-explosion accretion phase* begins when energy deposition by ν -heating in the post-shock layers becomes sufficiently strong so that the total energy in the post-shock region ultimately becomes positive. During this phase the shock accelerates outward while gas is still accreted onto the PNS. This process is commonly called “shock revival”. The duration of the latter two phases depends on the progenitor. During the *post-accretion phase*, the fourth and final phase characterizing the evolution of our models, accretion ends and the proto-neutron star develops a nearly spherical neutrino-driven wind.

During the quasi-spherical shock expansion phase shortly after bounce the level of temporal and angular fluctuations of the neutrino emission is small ($\lesssim 10^{-2}$). In contrast, the fluctuation amplitudes reach a level of several 10% of the average values during the hydrodynamically vigorous pre-explosion phase and the post-explosion accretion phase, where a few distinct, highly time-variable regions or even short-lived single spots with an angular size of 10° to 20° are responsible for the brightest emission maxima. As the outward shock expansion is well on its way in the post-explosion accretion phase, still existing accretion downdrafts can be responsible for similar fluctuations in the neutrino emission, though the number of corresponding hot spots decreases with diminishing accretion. When accretion has ended and the post-accretion phase has started, directional variations can be caused by the occurrence of Ledoux convection in the outer layers of the proto-neutron star, which we indeed observe

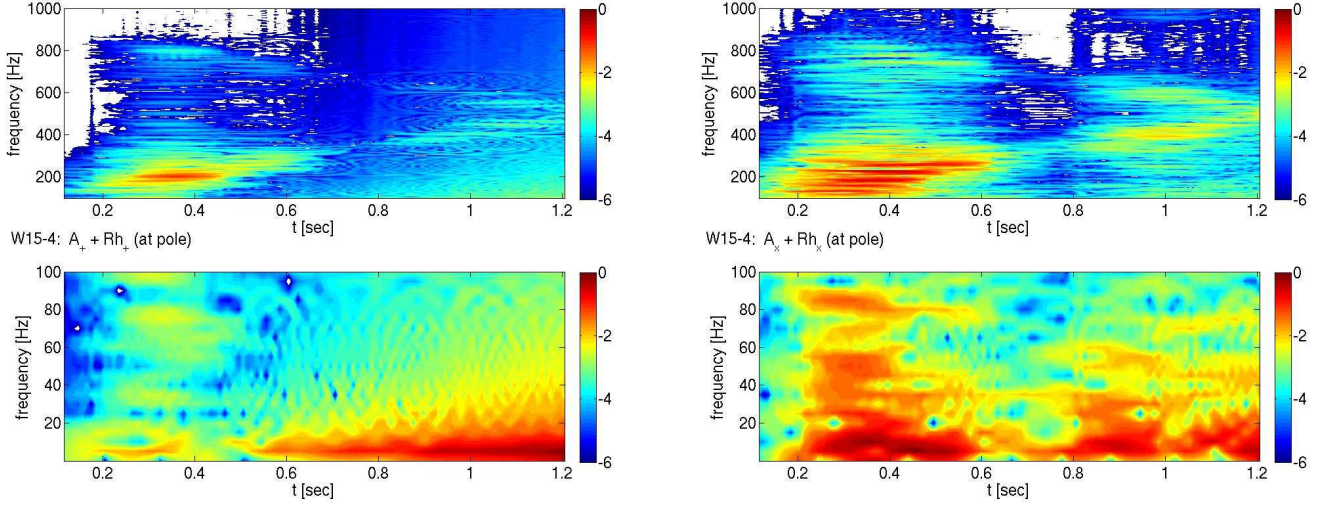


Fig. 17. Normalized (to the absolute maximum) amplitude spectrograms of the total gravitational wave amplitudes $A_+ + Rh_+$ (left panels) and $A_\times + Rh_\times$ (right panels) at the pole for model W15-4. The lower panels show the spectrograms in the frequency range 5 Hz to 100 Hz, and the upper ones in the frequency range 100 Hz to 1 kHz.

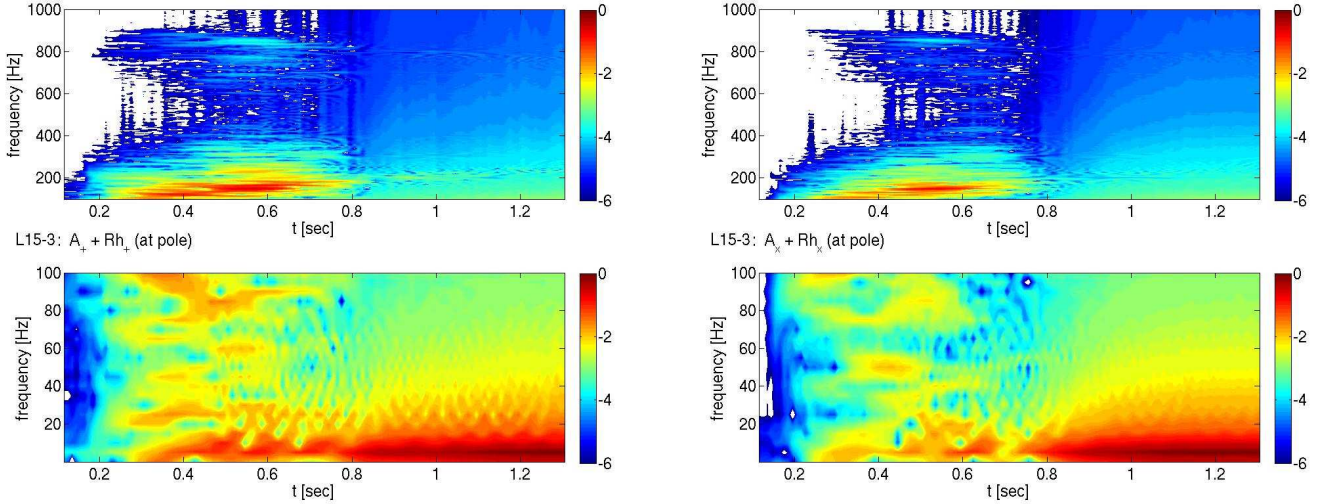


Fig. 18. Same as Fig. 17, but for model L15-3.

in models based on two of our three progenitors (see also the discussion of the influence of the inner radial boundary condition below). The temporal and angular variations of the emission in different directions are even more pronounced when considering the energy flux of the electron neutrinos or electron anti-neutrinos alone (instead of the emission in all neutrino flavors). In that case the angular variations of local flux densities can exceed 100% in all models during the pre-explosion and post-explosion accretion phases, and the peak values can be close to 200% during short episodes. The total energy loss rates in neutrinos and the observable luminosities as surface-integrated quantities, however, are much smoother in time during all phases, showing fluctuation amplitudes of at most several percent.

The gravitational wave emission also exhibits the generic time-dependent features already known from 2D (axisymmetric) models, but the 3D wave amplitudes are considerably smaller (by a factor of 2 – 3) than those predicted by 2D models (Müller et al. 2004; Marek et al. 2009; Murphy et al. 2009;

Yakunin et al. 2010) due to less coherent mass motions and neutrino emission. Note in this respect that the GW quadrupole amplitudes which are usually quoted for 2D models (A_{20}^{E2}) have to be multiplied by a geometric factor $\sin^2 \theta \sqrt{15/\pi}/8$ (which is equal to ≈ 0.27 for $\theta = 90^\circ$). Violent, non-radial hydrodynamic mass motions in the accretion layer and their interaction with the outer layers of the proto-neutron star give rise to a GW signal with an amplitude of $\sim 2 - 4$ cm in the frequency range of ~ 100 Hz to ~ 400 Hz, while anisotropic neutrino emission is responsible for a superimposed low-frequency evolution of the wave amplitude, which thus can grow to maximal values of 10 – 20 cm. Variations of the mass-quadrupole moment due to convective activity inside the nascent neutron star contribute a high-frequency component (300 – 600 Hz) to the GW signal during the post-accretion phase. The GW signals exhibit strong variability between the two polarizations, different explosion simulations and different observer directions, and besides common basic features do not possess any template character.

Finally we would like to reflect some of the deficiencies of the presented 3D models. Due to the ray-by-ray treatment of the ν -transport the directional variations of the neutrino emission in response to local inhomogeneities in the star may be over-estimated (Ott et al. 2008; Brandt et al. 2011). However, when we evaluate observable signals, such artificial effects are mostly compensated for by integrations of the neutrino flux densities over the surface areas visible to observers from different viewing directions (see Eqs. 5, 7, 10, 11), or by the integration of the neutrino energy loss into all directions (Eqs. 13, 53).

Another deficiency concerns the usage of the inner radial grid boundary, because of which our simulations do not fully include (neither in space nor time) the convective flow occurring in the PNS interior after core bounce (Keil et al 1996; Buras et al. 2006; Dessart et al. 2006). Moreover, convective activity in the simulated outer layers of the PNS is triggered only when the artificially imposed inflow of neutrino energy and lepton number through the inner radial boundary into the adjacent layers is faster than neutrino transport (on the computational grid) can carry away this energy or lepton number. Whether this is the case sensitively depends on the employed neutrino-transport approximation, but also on the location and contraction of the grid boundary, the chosen values of the boundary luminosities, and on the stellar progenitor. Its mass-infall rate decides about how much mass accumulates in the near-surface layers of the PNS outside the inner grid boundary. As the position of and the conditions imposed at the inner boundary can thus influence the neutrino emission properties, in particular during the post-accretion phase, our respective model predictions must be considered with care. While they do not allow to make any definite statements concerning the detailed neutrino signal of a particular progenitor model due to the neglected treatment of the inner parts of the proto-neutron star, the models nevertheless show that convective flows below the neutrinosphere are likely to imprint themselves on the neutrino emission, and hence also on the GW signal of core collapse supernovae. A measurement of these signals may actually provide some insight in the conditions inside proto-neutron stars.

Acknowledgements. This work was supported by the Deutsche Forschungsgemeinschaft through the Transregional Collaborative Research Centers SFB/TR 27 “Neutrinos and Beyond” and SFB/TR 7 “Gravitational Wave Astronomy” and the Cluster of Excellence EXC 153 “Origin and Structure of the Universe” (<http://www.universe-cluster.de>).

References

- Arcones, A., Janka, H.-T. & Scheck, L. 2007, *A&A*467, 1227
 Baade, W., & Zwicky, F. 1934, *Phys. Rev.* 45, 138
 Blanchet, L., Damour, T. & Schäfer, G. 1990, *MNRAS*242, 289
 Brandt, T.D., Burrows, A., Ott, C.D. & Livne, E. 2011, *ApJ*728, 8
 Buras, R., Janka, H.-Th., Rampp, M. & Kifonidis, K. 2006, *A&A*457, 281
 Burrows, A., & Hayes, J. 1996, *Phys. Rev. Lett.*76, 352
 Burrows, A., Hayes, J. & Fryxell, B.A. 1995, *ApJ*450, 830
 Cerda-Duran, P., Faye, G., Dimmelmeier, H., Font, J.A., Ibanez, J.M., Müller, E. & Schäfer, G. 2005, *A&A*439, 1033
 Colella, P. & Glaz, H.M. 1985, *J. Chem. Phys.*59, 264
 Collella, P. & Woodward, P.R. 1984, *J. Chem. Phys.*54, 174
 Dessart, L., Burrows, A., Livne, E. & Ott, C.D. 2006, *ApJ*645, 534
 Dimmelmeier, H., Font, J.A. & Müller, E. 2001, *ApJ*560, L163
 Dimmelmeier, H., Font, J.A. & Müller, E. 2002, *A&A*393, 523
 Dimmelmeier, H., Ott, C.D., Janka, H.-T., Marek, A. & Müller, E. 2007, *Phys. Rev. Lett.*98, 01101
 Dimmelmeier, H., Ott, C.D., Marek, A. & Janka, H.-T. 2008, *Phys. Rev. D*78, 064056
 Epstein, R. 1978, *ApJ*223, 1037
 Finn, L.S. & Evans, C.R. 1990, *ApJ*351, 588
 Fryer, C.L. 2004, *ApJ*601, L175
 Fryer, C.L. & New, K.C.B. 2011, *Living Rev. Relativity* 14, (2011), 1, <http://www.livingreviews.org/lrr-2011-1>
 Fryer, C.L., Holz, D.E. & Hughes, S.A. 2004, *ApJ*609, 288
 Fryxell, B., Müller, E. & Arnett, D. 1991, *ApJ*, 367, 619
 Heger, A., Woosley, S.E., & Spruit, H.C. 2005, *ApJ*, 626, 350
 Janka, H.-T. & Mönchmeyer, R. 1989a, *A&A*209, L5
 Janka, H.-T. & Mönchmeyer, R. 1989b, *A&A*226, 69
 Janka, H.-T. & Müller, E. 1996, *A&A*306, 167
 Kageyama, A. & Sato, T. 2004, *Geochemistry Geophysics Geosystems* 5, Q09005
 Keil, W., Janka, H.-T. & Müller, E. 1996, *ApJ*473, L111
 Kotake, K., Yamada, S. & Sato, K. 2003, *Phys. Rev. D*68, 44023
 Kotake, K., Yamada, S., Sato, K., Sumiyoshi, K., Ono, H. & Suzuki, H. 2004, *Phys. Rev. D*69, 124004
 Kotake, K., Yamada, S. & Sato, K. 2005, *ApJ*618, 474
 Kotake, K., Sato, K. & Takahashi, K. 2006, *Rep. Prog. Phys.* 69, 971
 Kotake, K., Onishi, N. & Yamada, S. 2007, *ApJ*655, 406
 Kotake, K., Iwakami, W., Ohnishi, N. & Yamada, S. 2009a, *ApJ*704, 951
 Kotake, K., Iwakami, W., Ohnishi, N. & Yamada, S. 2009b, *ApJ*697, L133
 Kotake, K., Iwakami Nakano, W. & Ohnishi, N. 2011, *ArXiv e-prints* 1106.0544
 Liebendörfer, M. 2005 *ApJ*633, 1042
 Liebendörfer, M., Whitehouse, S.C. & Fischer, T. 2009 *ApJ*698, 1174
 Limongi, M., Straniero, O. & Chieffi, A. 2000, *ApJS*129, 625
 Liou, M.S. 1996, *J. Chem. Phys.*129, 364
 Lund, T., Marek, A., Lunardini, C., Janka, H.-Th. & Raffelt, G. 2010, *Phys. Rev. D*82, 063007
 Marek, A. & Janka, H.-Th. 2009, *ApJ*694, 664
 Marek, A., Dimmelmeier, H., Janka, H.-Th., Müller, E. & Buras, R. 2006, *A&A*445, 273
 Marek, A., Janka, H.-Th. & Müller, E. 2009, *A&A*496, 475
 Misner C.W., Thorne K.S., Wheeler J.A., 1973, *Gravitation*, chap. 35, Freeman, San Francisco, USA
 Mönchmeyer, R., Schäfer, G., Müller, E. & Kates, R. 1991, *A&A*246, 417
 Müller, B., Dimmelmeier, H. & Müller, E. 2008, *A&A*489, 301
 Müller, E. 1982, *A&A*114, 53
 Müller, E. & Steinmetz, M. 1995, *Comp. Phys. Comm.*, 89, 45
 Müller, E. & Janka, H.-Th. 1997, *A&A*317, 140
 Müller, E., Fryxell, B. & Arnett, D. 1991a, *A&A*, 251, 505
 Müller, E., Fryxell, B., & Arnett, D. 1991b, in *European Southern Observatory Conference and Workshop Proceedings*, Vol. 37, ed. I. J. Danziger & K. Kjaer, 99
 Müller, E., Rampp, M., Buras, R., Janka, H.-Th. & Shoemaker, D.H. 2004, *ApJ*603, 221
 Murphy, J.W., Ott, C.D. & Burrows, A. 2009, *ApJ*707, 1173
 Nakamura T., Oohara K. 1989, in: *Frontiers in Numerical Relativity*, eds. C.R. Evans, L.S. Finn, and D.W. Hobill, Cambridge Univ. Press, p. 254
 Obergaulinger, M., Aloy, M.A. & Müller, E. 2006a, *A&A*450, 1107
 Obergaulinger, M., Aloy, M.A. & Müller, E. 2006b, *A&A*457, 209
 Oohara, K., Nakamura T. & Shibata. M. 1997, *Prog. Theor. Phys. Suppl.* 128, 183
 Ott, C.D. 2009, *Class. Quant. Grav.* 26, 063001
 Ott, C.D., Burrows, A., Livne, E. & Walder, R. 2004, *ApJ*600, 834
 Ott, C.D., Burrows, A., Dessart, L. & Livne, E. 2006, *Phys. Rev. Lett.*96, 201102
 Ott, C.D., Dimmelmeier, H., Marek, A., Janka, H.-T., Zink, B., Hawke, I. & Schnetter, E. 2007, *Phys. Rev. Lett.*98, 261101
 Ott, C.D., Burrows, A., Dessart, L. & Livne, E. 2008, *ApJ*685, 1069
 Ott, C.D., Reisswig, C., Schnetter, E., O’Connor, E., Sperhake, U., Loeffler, F., Diener, P., Abdikamalov, E., Hawke, I. & Burrows, A. 2010, *ArXiv e-prints* 1012.1853
 Pejcha, O. & Thompson, T.A. 2011, *ArXiv e-prints* 1103.4864P
 Plewa, T. & Müller, E. 1999, *A&A*, 342, 179
 Quirk, J.J. 1994, *Int. J. Num. Meth. Fluids* 18, 555
 Rampp, M., Müller, E. & Ruffert, M. 1998, *A&A*332, 969
 Rampp, M. & Janka, H.-T. 2002, *A&A*396, 361
 Saijo, M. 2006, *Phys. Rev. D*71, 104038
 Scheck, L., Kifonidis, K., Janka, H.-T., & Müller, E. 2006, *A&A*457, 963
 Scheidegger, S., Fischer, T., Whitehouse, S.C. & Liebendörfer, M. 2008, *A&A*490, 231
 Scheidegger, S., Käppeli, R., Whitehouse, S.C., Fischer, T. & Liebendörfer, M. 2010, *A&A*514, A51
 Shibata, M. 2003, *Phys. Rev. D*67, 024033
 Shibata, M. & Sekiguchi, Y. 2004, *Phys. Rev. D*69, 084024
 Shibata, M. & Sekiguchi, Y. 2005, *Phys. Rev. D*71, 024014
 Shigeyama, T. & Nomoto, N. 1990, *ApJ*360, 242
 Strang, G. 1968, *SIAM J. Numer. Anal.* 5, 506
 Wongwathanarat, A. 2011, *PhD thesis*, Technical University Munich
 Wongwathanarat, A., Hammer, N.J. & Müller, E. 2010a, *A&A*514, A48
 Wongwathanarat, A., Janka, H.-T. & Müller, E. 2010b, *ApJ*725, L106

- Wongwathanarat, A., Janka, H.-T. & Müller, E. 2011, A&A, to be submitted
- Woosley, S.E. & Weaver, T.A. 1995, ApJS101, 181
- Yakunin, K.N., Marronetti, P., Mezzacappa, A., Bruenn, S.W., Lee, C.-T., Chertkow, M.A., Hix, W.R., Blondin, J.M., Lentz, E.J., Bronson Messer, O.E & Yoshida, S. 2010, *Class. Quant. Grav.* 27, 194005
- Yamada, S. & Sato, K. 1994, ApJ450, 245
- Yamada, S. & Sawai, H. 2004, ApJ608, 907
- Zwerger, T. & Müller, E. 1997, A&A, 320, 209